JGR Solid Earth

RESEARCH ARTICLE

10.1029/2024JB029820

# Subsurface Imaging in Urban Areas With Ambient Noise Using DAS and Seismometer Data Sets: Granada, Spain

**B. Benjumea**[1], **B. Gaite**[2], **M. Schimmel**[3], **F. Bohoyo**[1], **Z. J. Spica**[4], **F. D. L. Mancilla**[5,6], **Y. Li**[4], **J. Almendros**[5,6], **and J. Morales**[5,6]

[1]Instituto Geológico y Minero de España-CSIC, Madrid, Spain, [2]Instituto Geográfico Nacional de España, Madrid, Spain, [3]Geosciences Barcelona (GEO3BCN-CSIC), Barcelona, Spain, [4]Department of Earth and Environmental Sciences, University of Michigan, Ann Arbor, MI, USA, [5]Instituto Andaluz de Geofísica, Universidad de Granada, Granada, Spain, [6]Departamento de Física Teórica y del Cosmos, Universidad de Granada, Granada, Spain

**Key Points:**

- Distributed Acoustic Sensing holds great potential for urban seismic data acquisition
- Autocorrelation and Microtremor Horizontal to Vertical Spectral Ratio methods consistently reveal bedrock depth exceeding 1,000 m in Granada
- A novel approach is developed to analyze autocorrelation results for retrieving subsurface reflections

**Correspondence to:**

B. Benjumea,
b.benjumea@csic.es

**Citation:**

Benjumea, B., Gaite, B., Schimmel, M., Bohoyo, F., Spica, Z. J., Mancilla, F. D. L., et al. (2024). Subsurface imaging in urban areas with ambient noise using DAS and seismometer data sets: Granada, Spain. *Journal of Geophysical Research: Solid Earth*, *129*, e2024JB029820. https://doi.org/10.1029/2024JB029820

Received 28 JUN 2024
Accepted 1 NOV 2024

**Author Contributions:**

**Conceptualization:** B. Benjumea
**Data curation:** Z. J. Spica, F. D. L. Mancilla, Y. Li
**Funding acquisition:** F. Bohoyo, Z. J. Spica
**Investigation:** F. Bohoyo, J. Almendros, J. Morales
**Methodology:** B. Benjumea, B. Gaite, M. Schimmel
**Resources:** B. Gaite, F. Bohoyo, Z. J. Spica
**Software:** B. Benjumea, M. Schimmel
**Supervision:** J. Almendros
**Validation:** B. Gaite, M. Schimmel, F. D. L. Mancilla
**Writing – original draft:** B. Benjumea
**Writing – review & editing:** B. Gaite, M. Schimmel, F. Bohoyo, Z. J. Spica, F. D. L. Mancilla, Y. Li, J. Almendros, J. Morales

© 2024. The Author(s).
This is an open access article under the terms of the Creative Commons Attribution-NonCommercial-NoDerivs License, which permits use and distribution in any medium, provided the original work is properly cited, the use is non-commercial and no modifications or adaptations are made.

## Abstract

Distributed acoustic sensing (DAS) is an innovative technology with great potential for acquiring seismic data sets in urban areas. In this work, we check the suitability of a DAS data set acquired in Granada (Spain) for retrieving subsurface reflectivity from ambient noise. The fiber-optic is a pre-existing underground telecommunication cable that crosses the city from Northwest to Southeast. We use a 10 hr recording of strain rate from a 2020 experiment to obtain seismic reflections using the autocorrelation method. We compare the DAS results with reflections obtained from seismic ambient noise recorded in nine seismometers deployed close to the fiber-cable for 7 days in November 2022. The novel approach proposed in this study for the identification of the reflections is to use autocorrelations after bandpass filtering for specific central frequencies and to check the stability of the signals over a broad frequency band. Microtremor Horizontal to Vertical Spectral Ratio (MHVSR) measurements at a total of 14 stations, five of them outside the city, help to constrain the reflection interpretation. These include one station at the borehole that reaches the basement in the Granada Basin crossing all the Cenozoic units. We use the legacy sonic log to obtain a relationship between frequencies of MHVSR peaks and depth. Autocorrelation and MHVSR methods give consistent results delineating bedrock depth deeper than 1,000 m in Granada. These results confirm that DAS can provide valuable subsurface information in urban areas.

## Plain Language Summary

Urban subsurface information is of paramount importance to understand how the underground affects the development of cities (groundwater or hazards such as earthquakes). One of the most useful methods to improve the knowledge of the city underground is seismic technique but installation of vibration sensors can be difficult in an urban area. We use in this work a cutting-edge technology called Distributed Acoustic Sensing (DAS) that uses fiber-optic cables in the city, such as preinstalled telecommunication cables, as a high number of seismic sensors. We compare the seismic results obtained from the measurements in the fiber-optic cable and from conventional seismometers. The analysis of the vibrations acquired with DAS and seismometers provide reflections, like echo signals, from the subsurface changes. In particular we obtain a reflection coming from the contact between sediments and bedrock. The depth of this contact is similar with the two type of measurements reaching 1,400 m depth below the city. This confirms that this new technology can be used in cities to study their subsurface.

## 1. Introduction

The technology of fiber optic Distributed Acoustic Sensing (DAS) has been expanding its applications in Seismology in recent years (Zhan, 2019). Examples include the detection of local earthquakes (Sladen et al., 2019) and teleseisms (e.g., Ajo-Franklin et al., 2019), the estimate of earthquake magnitude and stress drop (e.g., Lior et al., 2021; Yin et al., 2023), the retrieval of hydroacoustic *T* waves (Ugalde et al., 2022) and surface waves (Spica, Nishida et al., 2020) to compute shear-wave velocity models of the subsoil. Studies like Farghal et al. (2022) and Lior et al. (2023) analyzed the potential of DAS in Earthquake Early Warning applications. Recently, an international initiative of simultaneous DAS recordings has been deployed to check its possible usage as a global seismic network (Wuestefeld et al., 2023). Overall, DAS is useful to compute the velocity structure of the subsoil under the fiber optic, specially in areas where a seismic profile or a seismic network is difficult to deploy. For example, deployments implying high costs, difficult access, or low level of security for the instruments. Therefore, DAS results in a convenient technique to retrieve seismic subsoil information in oceans (e.g., Spica, Nishida et al., 2020), volcanoes (e.g., Biagioli et al., 2024; Currenti et al., 2023) and urban areas (Dou et al., 2017; Fang et al., 2020; Spica, Perton et al., 2020), where fiber optic is already deployed and available. Despite its easy arrangement, its large aperture and its high-density sampling when using an already deployed fiber that is was installed for other purposes, DAS recording implies some difficulties to retrieve the seismic information. Indeed, sometimes only some channels of the whole fiber length are sensitive to the seismic wavefield due to uneven cable-ground coupling reducing significantly the number of sensors (Li et al., 2023).

In general, DAS has a lower signal-to-noise ratio and a more limited angular sensitivity than standard seismometers; however, this drawback is largely compensated by the benefits of having an ultra-dense series of permanently installed and highly resistant seismic sensors communicating over large distances and running on a single power source (Martin, 2018).

Because strain rate is a tensor quantity, the response of fiber optic systems to ground shaking is more complex than that of conventional seismometers. Furthermore, DAS measures the linear strain rate with only one component along the fiber, meaning it has a direction-dependent sensitivity to different seismic waves (Martin et al., 2021). In addition, the ground coupling may not be as good as for traditional seismometers and its effects on the reliability of the waveforms and amplitudes are still uncertain although somewhat quantifiable (Lindsey et al., 2020).

Due to these all drawbacks, it is useful to compare DAS results to conventional seismometers as control purpose and to reduce ambiguities.

Passive seismic interferometry has been widely used to image the subsoil for the last two decades at different scales and depths (e.g., Bensen et al., 2008; Gaite et al., 2012 and references therein; Lin et al., 2008; Shapiro & Campillo, 2004; Stehly et al., 2009; Yao et al., 2006).

The dominance of surface waves in ambient noise records has enabled the imaging of shallow Earth properties with shear-wave velocity profiles using seismometers, as demonstrated by Brenguier et al. (2007), Calò et al. (2023), Kruiver et al. (2017), and Yang et al. (2011). Similarly, several authors have employed DAS ambient noise measurements to derive surface waves dispersion images through cross-correlation techniques, showing that the phase is well retrieved with DAS (Spica, Perton et al., 2020; Zeng et al., 2017).

Surface waves dominance makes it challenging to retrieve information on P-waves and their reflections from the ambient noise record. However, some studies have retrieved P-waves from ambient noise with good results (e.g., Draganov et al., 2007, 2009; Nakata et al., 2015; Poli et al., 2012). Autocorrelations of ambient noise seem to be a valuable tool to image P-wave reflections at different impedance contrasts beneath a seismic station (e.g., Clayton, 2020; Romero & Schimmel, 2018), and even to monitor velocity changes of the subsoil (e.g., Ugalde et al., 2014 or Qin et al., 2023). DAS autocorrelations produce subsurface reflection images beneath the fiber, having the advantage of the easy deployment and maintenance of the DAS interrogator (e.g., Lior et al., 2022; Spica, Nishida et al., 2020). To the best of our knowledge, seismic reflection observations through the autocorrelation of DAS measurements had not been achieved until the present study.

Another technique that uses ambient noise to retrieve subsurface information is the Microtremor Horizontal-to-Vertical Spectral Ratio (MHVSR) method. The shape of the MHVSR curve can be associated with the presence of seismic impedance contrasts. The underlying principles of this method have sparked debate (Bonnefoy-Claudet et al., 2006). Some researchers have established a direct connection between the shape of MHVSR curves and subsurface S-wave resonance (Nakamura, 2000). In contrast, others have proposed that the MHVSR curve's shape is influenced by the polarization of surface waves (e.g., Konno & Ohmachi, 1998). In the past decade, Sánchez-Sesma et al. (2011) proposed that comprehending the physical foundations of seismic noise necessitates viewing it as a diffuse wavefield encompassing all types of elastic waves. In this sense, Perton et al. (2018) stated that even complex velocity structure can be retrieved from the MHVSR. However, the main application is to relate the frequency of the MHVSR curve maximum with the depth of the acoustic impedance contrast (e.g., Macau et al., 2018).

Cities are complex systems that exist at the interface of natural, built and social environments. Geological insights into the subsurface are crucial for sustainable development (related to groundwater or geoenergy), responsible urban planning and resilience against geohazards. Geophysical methods can play an important role in for comprehending the physical properties, structure and processes that affect the urban subsurface. Applying

21699356, 2024, 11, Downloaded from https://agupubs.onlinelibrary.wiley.com/doi/10.1029/2024JB029820 by California Institute Of Techno, Wiley Online Library on [12/11/2025]. See the Terms and Conditions (https://onlinelibrary.wiley.com/terms-and-conditions) on Wiley Online Library for rules of use; OA articles are governed by the applicable Creative Commons License

geophysical methods in urban settings encounters various difficulties, such as environmental noise (both seismic and electromagnetic) and logistical limitations (including restricted open spaces and the complexity of setting up instrumentation). To address these challenges, it is crucial to focus research efforts on both data acquisition and methods. As mentioned before, DAS presents a great potential for seismic data acquisition in urban studies (Spica, Perton et al., 2020). On the other hand, ambient noise methods are suitable for urban subsurface characterization (Macau et al., 2018).

This work aims to check the suitability of getting subsurface information from autocorrelation of ambient noise recorded using a fiber-optic telecom cable in the city of Granada (Spain). The information is compared to the one obtained with seismometers located across the city and using autocorrelation and MHVSR techniques. For both data sets, the methodology has been tailored to extract useful information from autocorrelations that have been contrasted with MHVSR results. The use of DAS, supported by seismometers, to obtain subsurface information from ambient noise analysis in the city of Granada can be adapted and used by other cities facing the complexities of urban underground studies.

## 2. Geological Setting

The city of Granada and its metropolitan area is in the eastern part of the Granada Basin, at southeast of the Iberian Peninsula (Figure 1a). The geomorphology of the Granada Basin is characterized by a plain relief, with altitudes that vary from 520 m at its westernmost limit to 650 m at its eastern border. The basin is surrounded by gentle slopes of alluvial fans along its southern and eastern border. Toward the north and east, there are successive masses of coarse detritus in different alluvial fans, accumulating since the Pliocene (Braga et al., 1990, 2003) that have been eroded by the Genil River and its subsidiaries (Chacón et al., 2012).

The Betic Cordillera together with the Rif (Northern Africa), constitute the westernmost alpine mountain belt in the Mediterranean area. The two mountain ranges are connected by the Gibraltar Arc and they surround the Alboran Sea (Figure 1; Madarieta-Txurruka et al., 2021). The Neogene-Quaternary evolution of the Granada Basin, one of the largest intermontane basins of the Betic Cordillera, occurs between the External and Internal Zones, the two main domains of the Cordillera. It is filled with middle Miocene to Quaternary sediments and is bounded on the E–SE side by the Sierra Nevada, the most elevated area of the mountain range reaching more than 3,400 m. Active deformation with a moderate level of seismicity is recorded (Lozano et al., 2022; Morales et al., 1997; Muñoz et al., 2002; Stich et al., 2020). This seismic deformation is mainly accommodated by an NE–SW extension (Mancilla et al., 2013; Martín et al., 2015) associated to a slow (4–5 mm/yr) NNW–SSE regional convergence between Nubia and Iberia tectonic plates (Nocquet, 2012; Palano et al., 2015; Serpelloni et al., 2007). The basin is bounded by a set of E–W, ENE–WSW to NE–SW strike-slip and normal faults at the northern and southern boundaries (Sanz de Galdeano et al., 2012) and particularly NE–SW and E–W fault sets develop half-graben structures with sediment tilting toward the NNW and defining the main subsiding areas in the eastern part of the basin (Rodríguez-Fernández & Sanz de Galdeano, 2006).

The basement of the basin in the Granada metropolitan area consists of metamorphic rocks (Alpujarride complex) of the Internal Zones, although the northwestern part of the basin has a basement composed of sedimentary rocks of the External Zones. From basement to top, five main depositional sequences are considered: (1) marine sediments (calcarenites, marls, conglomerates, and sands) of Serravallian and late Tortonian age. (2a) thick evaporitic deposits (gypsum and salt) in the southern part of the basin, related to the final retreat of the sea in the latest Tortonian-Messinian, while in the northeastern part, clastic sediments (sand and silts) deposited by large alluvial fans. (2b) lacustrine limestones in the western part that was partially occupied by lakes during late Messinian (3a) fluvial conglomerates, sands and clays, and lacustrine limestones were deposited during the Pliocene. These include the local “Alhambra Formation”, which is composed of thick detrital sedimentary conglomerates associated with alluvial fans of the basal Pliocene (3b). Finally, the current alluvial plain formed during the Pleistocene when the major Guadalquivir River drainage system, including Genil River, captured the basin (Madarieta-Txurruka et al., 2021; Rodríguez-Fernández & Sanz de Galdeano, 2006).

An approach to the local site amplification in the city of Granada has been addressed by Alguacil et al. (2012) using acceleration records from the very deep earthquake of 11 April 2010 ($h = 613$ km) of $Mw = 6.3$ occurred with epicenter close to Granada city. Alguacil et al. (2012) apply spectral ratio and H/V techniques, in the 1–10 Hz band, to acceleration records obtained in four locations in the capital of Granada and a broadband record taken as a

21699356, 2024, 11, Downloaded from https://agupubs.onlinelibrary.wiley.com/doi/10.1029/2024JB029820 by California Institute Of Techno, Wiley Online Library on [12/11/2025]. See the Terms and Conditions (https://onlinelibrary.wiley.com/terms-and-conditions) on Wiley Online Library for rules of use; OA articles are governed by the applicable Creative Commons License

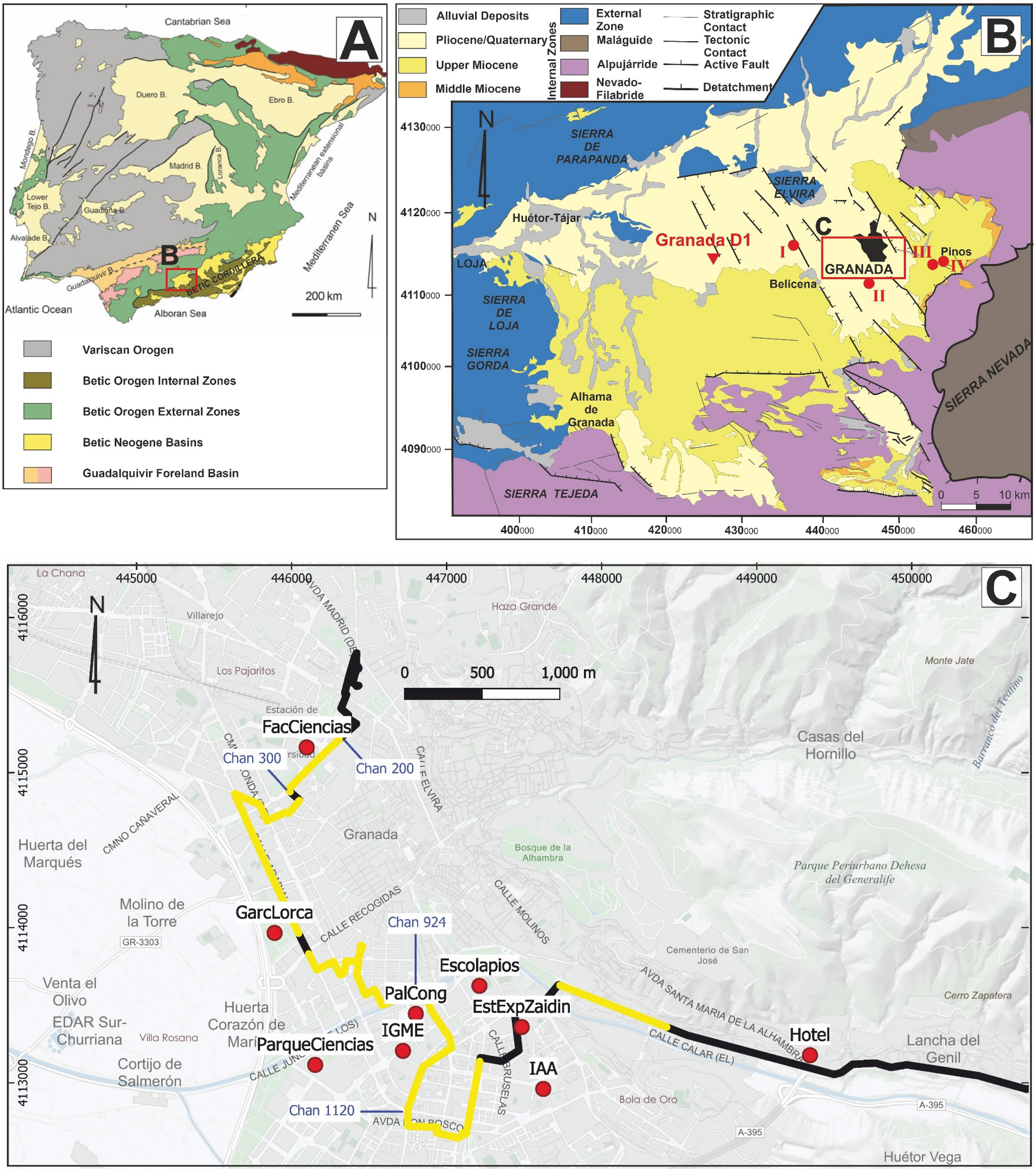

**Figure 1.** (a) Location of Granada basin (red rectangle) in the Iberian Peninsula geological map (modified from Braga and Cunha (2019)). (b) Geological map of the Granada basin (modified from Sanz de Galdeano et al. (2012)). The city of Granada is highlighted with a black shape. Five seismometers are located outside the city of Granada. Four of them are denoted as red circles and labeled with roman numbers I-IV. The fifth one is located at the Granada-D1 borehole indicated with an inverted red triangle. (c) Location of underground fiber-optic cable in the city of Granada (black and yellow line). Yellow lines show the sections of the fiber cable that are analyzed in this work. Numbers along the cable indicate the positions of the sector limits shown in Figure 7. Red dots indicate three-component seismometer locations. Coordinates are UTM ETRS89 zone 30N.

21699356, 2024, 11, Downloaded from https://agupubs.onlinelibrary.wiley.com/doi/10.1029/2024JB029820 by California Institute Of Techno, Wiley Online Library on [12/11/2025]. See the Terms and Conditions (https://onlinelibrary.wiley.com/terms-and-conditions) on Wiley Online Library for rules of use; OA articles are governed by the applicable Creative Commons License

reference station, observing amplifications between 1 and 2 Hz according to the sediments involved in the subsurface of the city of Granada.

Prominent reflections in the legacy seismic profiles, indicative of major seismic unconformities, are identified throughout the basin infill. These reflections, correlated along the basin, occur between the basement and the Upper Miocene marine sediments (sequence 1), between the Upper Miocene marine sediments and the Upper Miocene continental sediments (sequences 2a and 2b), and finally, between the Upper Miocene continental sediments and the Pliocene to Quaternary sediments (sequences 3a and 3b) (Morales et al., 1990; Rodríguez-Fernández & Sanz de Galdeano, 2006). The position of the main depocenters determined by Morales et al. (1990) and later by Rodríguez-Fernández and Sanz de Galdeano (2006) is largely coincident, although the estimation of the sedimentary infill is greater in the first study reaching the 1,100 m of thickness in the city of Granada. Both studies estimated bedrock depth in the urban area by interpolating the information from seismic profiles acquired outside the city. Different velocity models using P-wave arrival times from local earthquakes were developed in the external zones and central part of the Betic Cordillera, including the Granada Basin (Serrano et al., 1998, 2002). However, these works were focused in imaging the cortical and upper mantle structure, not revealing the shallow subsurface structure, which is the target of our work.

New detailed gravimetric data delineate with greater precision the position of the depocenter of the Granada Basin near Granada city, coinciding with the minimum of the Bouguer anomaly, and estimate fill thicknesses of up to approximately 1,400–1,600 m, based on gravimetric modeling (Madarieta-Txurruka et al., 2021).

The Granada-D1 Borehole situated at the central part of the basin at 641 m above sea level (Figure 1b) penetrates 841 m, recovering all the Miocene-Pleistocene sedimentary infill and reaching older Mesozoic rocks (Jurassic and Triassic). This borehole is representative of the geological architecture of the basin and the only one nearest to the city with acoustic logging.

Figures 2a and 2b show two well logs from this borehole: natural gamma log and P-wave velocity ($V_p$), respectively. The synthetic lithological composite log is displayed in Figure 2d. We calculate the 5-m interval velocity from the P-wave log (blue line in Figure 2c) and obtain an estimate of the S-wave velocity ($V_s$) from this interval velocity using the Brocher relationship (Brocher, 2005). The sonic log is not available for the first 200 m, which is usually associated with unstable borehole conditions (unconsolidated sediments) that require casing. This precludes logging with the sonic tool, which only works in open boreholes. These unconsolidated sediments are probably associated with low shear wave velocities. Miocene sediments below 200 m are characterized by $V_p$ in the range of 2,000–2,500 m/s (estimated $V_s$ between 700 and 1,000 m/s) with a smooth velocity increase with depth down to 580 m. A higher velocity layer lies below these sediments corresponding to the calcarenites of the sequence 1. Velocity logs indicate a significant increase in velocity around 600 m associated with the Cretaceous limestones from the External Zones that form the seismic basement at this location. Alternating low and high-velocity layers within 3,000–5,000 m/s (estimated $V_s$ 2,000–3,000 m/s) characterize the deeper part of the borehole related to the older Mesozoic rocks.

## 3. Data Acquisition

### 3.1. Distributed Acoustic Sensing: The GranaDAS Array

Distributed Acoustic Sensing (DAS) is emerging as a valuable tool for urban seismology (e.g., Li et al., 2023; Shragge et al., 2021; Spica, Perton et al., 2020). This rapidly advancing technology transforms conventional telecommunication fiber-optic cables into expansive and ultra-dense seismic arrays. At its core, a DAS interrogator is an optoelectrical device that sends repeated laser pulses into a fiber. A portion of the light is backscattered to the interrogator due to optical imperfections existing in the fiber. External disturbances, such as seismic or acoustic waves, induce phase shifts in the backscatter light. These shifts are then measured by an interferometer in the interrogator. They are directly proportional to the overall strain (or strain rate) along a section of the fiber (i.e., the gauge length). For an in-depth explanation of the DAS technology, readers are encouraged to consult Hartog (2017).

The fiber-optic cable employed in this study is under the operation of the IRAM (Instituto de Radioastronomía Milimétrica) and facilitates continuous telecommunication between the radio-telescope situated atop the Sierra Nevada and its central headquarters in Granada (see Figure 1 in Li et al., 2023). Under normal operation, the cable has no additional available fibers (i.e., dark fibers). Consequently, we connected a Febus Optics A1-R interrogator

21699356, 2024, 11, Downloaded from https://agupubs.onlinelibrary.wiley.com/doi/10.1029/2024JB029820 by California Institute Of Techno, Wiley Online Library on [12/11/2025]. See the Terms and Conditions (https://onlinelibrary.wiley.com/terms-and-conditions) on Wiley Online Library for rules of use; OA articles are governed by the applicable Creative Commons License

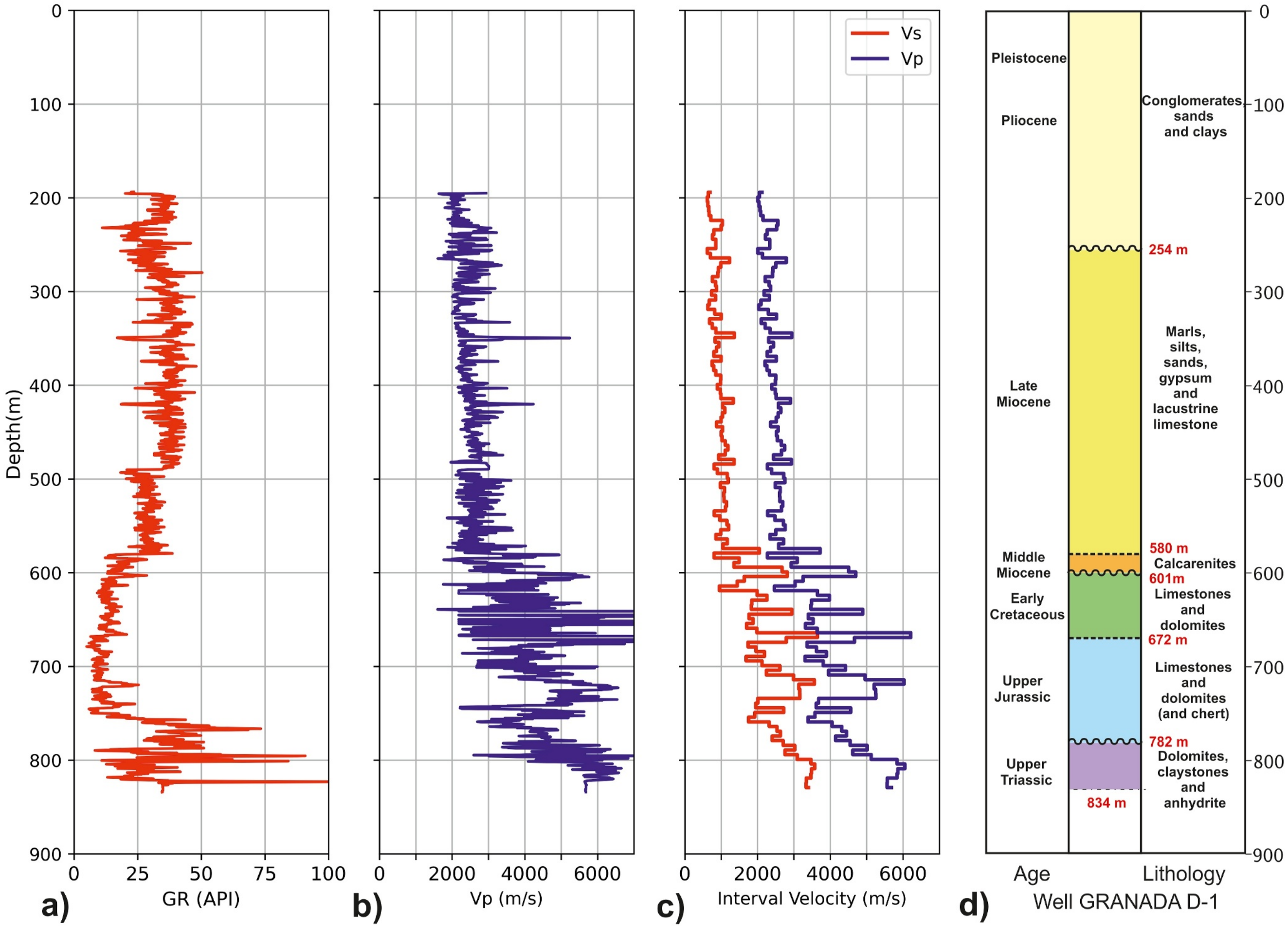

**Figure 2.** Granada-D1 borehole geophysical logging: (a) gamma-ray logging (b) P-wave velocity from sonic logging (c) 5 m interval velocity where blue line corresponds to P-wave velocity and red line to S-wave velocity. $V_s$ is calculated from the $V_p$–$V_s$ relationship from Brocher (2005) of Equation 3. (d) scheme of the lithological description of the borehole. Granada-D1borehole is located 16 km from the city of Granada (Figure 1b). 0 m indicates ground level.

to the fiber during the maintenance period of the radio-telescope, which occurred between 26 and 27 August, 2020. Throughout this period, we gathered approximately 19 hr of strain rate data at a sampling rate of 2,000 Hz. Except for the interruption at night when the radio telescope was operational, the setup recorded data along the initial 20 km of the fiber from central headquarters. The recording consisted of 4,167 channels spaced at 4.8-m intervals, with a gauge length of 9.6 m.

The GranaDAS array crosses various neighborhoods in Granada city before ascending the eastern slopes of Sierra Nevada Mountain (see Figure 1 in Li et al., 2023). The fiber installation report offers a detailed fiber location, typically positioned underneath the sides of roads. However, the report does not mention the presence of fiber slack loops in manholes, implying that the fiber is stretched between the IRAM and the radio-telescope. Consequently, the location of each channel has been interpolated based on recording parameters, introducing a moderate degree of uncertainty in the assigned channel geolocations. Furthermore, the coupling conditions of the fiber with the ground remain unknown. In this work, we focus on the fiber-optic cable segment located within the city of Granada (from Channel 1 to 1,560).

### 3.2. Seismometers

We performed a new seismic survey in November 2022 in and around Granada city (Figures 1b and 1c) with conventional three-component 20s Trillium Compact Horizon seismometers and Pegasus dataloggers. The sampling frequency was 200 Hz. Data collection lasted 7 days for the stations set up in the city. Our survey spans nine sites situated within Granada City. They are Facultad de Ciencias (FacCiencias), García Lorca House

21699356, 2024, 11, Downloaded from https://agupubs.onlinelibrary.wiley.com/doi/10.1029/2024JB029820 by California Institute Of Techno, Wiley Online Library on [12/11/2025]. See the Terms and Conditions (https://onlinelibrary.wiley.com/terms-and-conditions) on Wiley Online Library for rules of use; OA articles are governed by the applicable Creative Commons License

21699356, 2024, 11, Downloaded from https://agupubs.onlinelibrary.wiley.com/doi/10.1029/2024JB029820 by California Institute Of Techno, Wiley Online Library on [12/11/2025]. See the Terms and Conditions (https://onlinelibrary.wiley.com/terms-and-conditions) on Wiley Online Library for rules of use; OA articles are governed by the applicable Creative Commons License

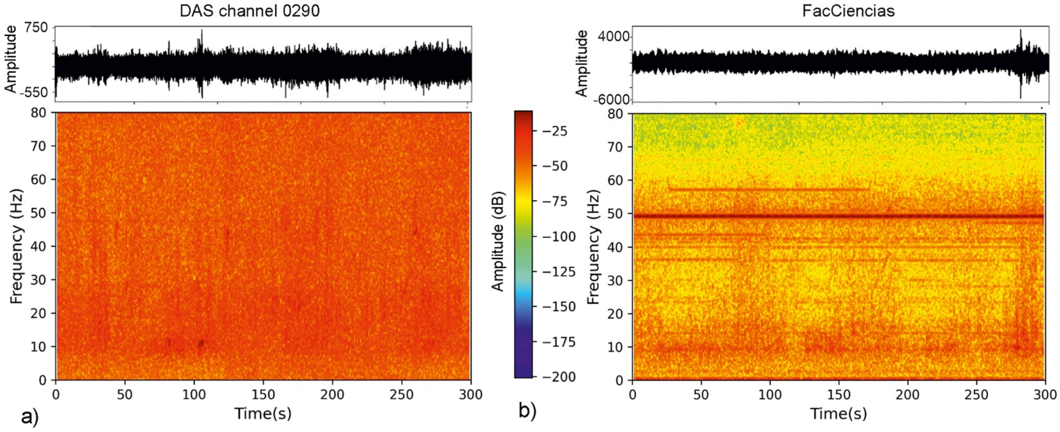

**Figure 3.** Five minutes record and corresponding spectrogram for DAS channel 290 (a) and the East component of FacCiencias seismometer. (b) 50 Hz electrical system noise is clearly detected at the FacCiencias seismometer.

Museum (GarcLorca), Parque de las Ciencias (ParqueCiencias), Instituto Geologico y Minero de España (IGME-CSIC) office in Granada (IGME), Palacio de Congresos (PalCong), Escolapios School (Escolapios), Estación Experimental del Zaidín-CSIC (EstExpZaidin), Instituto de Astrofísica de Andalucía-CSIC (IAA) and Hotel Macià Real de la Alhambra (Hotel) (Figure 1c). We installed the sensors on the ground floor or basement of buildings in contact with natural terrain in proximity to the fiber-optic cable.

In addition, we took five microtremor measurements outside the city. One was carried out at the Granada-D1 borehole, which is located 16 km from the city center (Figure 1b). This measurement aimed to obtain an MHVSR curve on the most representative borehole that crosses all the units reaching the Cenozoic base in the Granada Basin. For this site as well as for Belicena site (I at Figure 1b) the record length was only 2 hr. This duration is enough for MHVSR curve calculation according to the criteria discussed in Molnar et al. (2022). The borehole data set includes geophysical well logging as shown in Figure 2. The other three locations (Figure 1b) were at Instituto Andaluz de Ciencias de la Tierra (IACT) (II), Cenes de la Vega (III), and Pinos Genil (IV) to have additional MHVSR curves for Granada basin and in the vicinity of the city. In these three sites, the record length was 7 days since they were set up at buildings with no security issues as the ones in open sites.

## 4. Methods

### 4.1. Autocorrelation Method

In this work, we apply the autocorrelation technique to both DAS and seismometer data sets to retrieve the reflectivity response of the subsurface or empirical Green's functions (e.g., Romero & Schimmel, 2018). We converted 10 hr (from 6:00 a.m. to 4:00 p.m.) of DAS records from HDF5 to SAC format at 2,000 Hz and downsampled it to 400 Hz to compute the autocorrelations. Data from seismometers were kept at 200 Hz. We segmented the whole record in 300-s windows with an overlap of 75 s for each DAS channel and vertical and horizontal components of the seismometers.

We applied a conventional workflow of the autocorrelation method that includes, before calculating the autocorrelation functions, filtering the raw record between 5 to 30 Hz (DAS data set) and 5–20 Hz (seismometer data set). The spectrograms of both data sets support the different frequency range (Figure 3). We applied phase cross-correlation (PCC) following Schimmel (1999) and Bonilla and Ben-Zion (2021) to obtain the autocorrelation functions for each filtered time window for a maximum correlation lag of 10 s. This time length extends by several seconds the expected two-way travel time for a basement reflection in the Granada basin.

Finally, to get the final Green function, we stacked the obtained autocorrelation functions using the time-frequency phase weighted stack algorithm with power 2 (tf-PWS, Schimmel & Gallart, 2007) that provides a stable noise response. We will refer to the result of this workflow as stack 1.

Since ambient noise recordings in urban environments contain human-generated noise that can contaminate the autocorrelation results, we tried several methods to identify seismic signals related to subsurface structures. Some

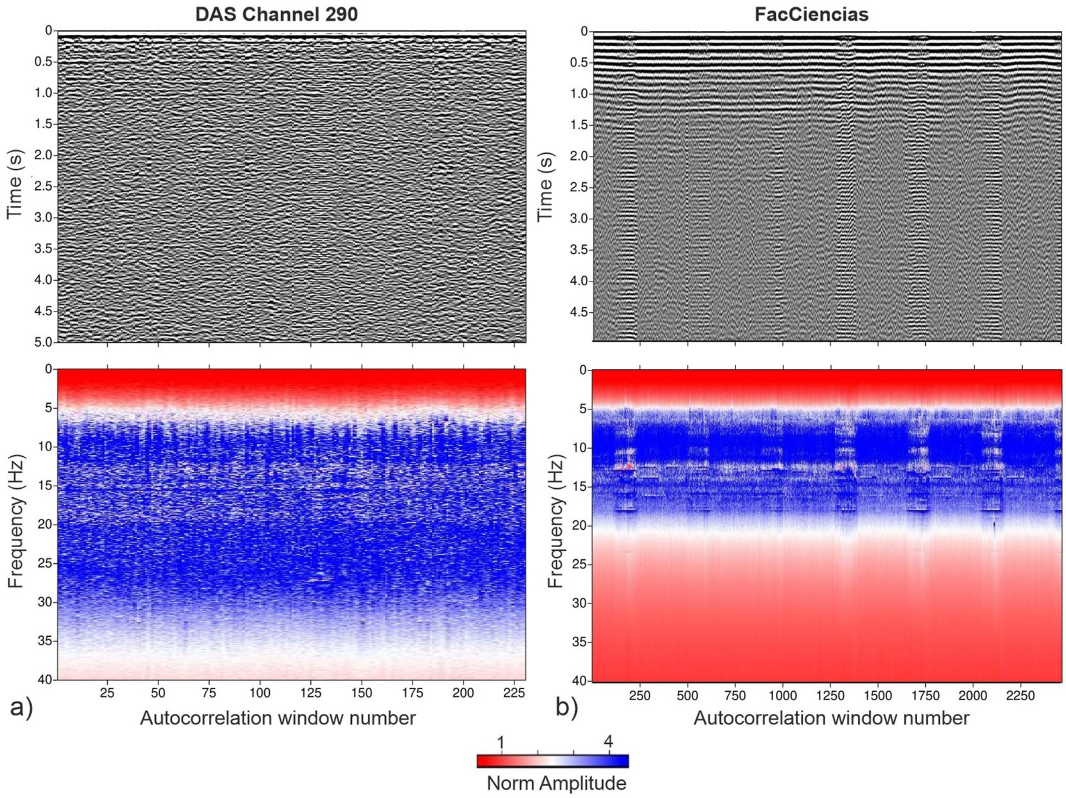

**Figure 4.** Stack of autocorrelations for each 5-min window and amplitude spectrum (a) for the recording of DAS channel 290 and (b) for a horizontal component of a nearby seismometer (FacCiencias). In both cases, black means positive polarity. Note that the number of windows for the seismometer is much higher than for DAS due to the different record length (7 days for FacCiencias, 10 hr for DAS). The autocorrelation computation includes a band pass filtering with frequency corners different for DAS and seismometers (5–30 Hz -DAS data set and 5–20 Hz -seismometer data set).

urban sources may produce recurring signals strong enough to appear in the autocorrelation stacks with significant amplitude.

Our first approach was to rely on the visual inspection of the calculated autocorrelations for all the windows and the corresponding amplitude spectra (Figure 4). We removed autocorrelations with ringing aspects in the time domain or anomalous amplitude spectra with distinct maxima. After stacking the kept autocorrelations, some remnant noise was still visible in the final stack showing this method was not suitable for our data set.

The second method tested is based on Schimmel et al. (2021). It consists of identifying the primary maximum in the amplitude spectrum of the autocorrelation stack. A notch filter around the corresponding frequency is applied to the data set before autocorrelation calculation, and then, the autocorrelation functions are stacked again. The process is repeated until the maxima are not present in the spectra of the final stack. In the Granada data set, we found a high number of spectrum maxima after autocorrelation stacking that precluded using this method.

The selected method to identify subsurface reflections is based on Castro-Artola et al. (2022) workflow, which examines the stability of autocorrelation functions across various frequencies. A set of central frequencies is defined and all the windows in the raw record are bandwidth filtered around these frequencies with an octave bandwidth (Table 1). Autocorrelation using phase correlation method and subsequent stacking are employed to obtain a stacked trace for different frequency bands defined by their central frequency. Plotting these traces as a function of central frequency can highlight stationary signals, that is, with the same polarity and aligned at the same lag time for different frequencies. This characteristic indicates a reflection phase since it is expected to mantain a constant lag time within a broad frequency band (Castro-Artola et al., 2022; Romero & Schimmel, 2018). The final stacked trace will be referred to as stack 2 in this work. This method was applied to DAS and seismometers data sets.

21699356, 2024, 11, Downloaded from https://agupubs.onlinelibrary.wiley.com/doi/10.1029/2024JB029820 by California Institute Of Techno, Wiley Online Library on [12/11/2025]. See the Terms and Conditions (https://onlinelibrary.wiley.com/terms-and-conditions) on Wiley Online Library for rules of use; OA articles are governed by the applicable Creative Commons License

**Table 1**
*Frequencies Used for Bandwidth Filters Before Autocorrelation and Stacking*

| Low frequency (Hz) | Central frequency (Hz) | High frequency (Hz) |
|---|---|---|
| 1.41 | 2.00 | 2.83 |
| 2.00 | 2.83 | 4.00 |
| 2.83 | 4.00 | 5.66 |
| 4.00 | 5.66 | 8.00 |
| 5.66 | 8.00 | 11.31 |
| 8.00 | 11.31 | 16.00 |
| 11.31 | 16.00 | 22.63 |
| 16.00 | 22.63 | 32.00 |

Figure 5 shows the stacked band-pass filtered autocorrelation functions in the left panels (stack 1). The center panels display the autocorrelation functions as a function of center frequency. The data have been band-passed filtered using a one-octave bandwidth and defined center frequency (see Table 1) before performing the autocorrelations and stacks. The right panels show the summed bandwidth filtered stacks corresponding to central frequencies from 4 to 16 Hz (stack 2). This frequency range was selected because the stacks corresponding to these central frequencies do not exhibit the noise observed in the other stacks. We show these results for the DAS channel number 300 (Figure 5a) and the two horizontal components of the nearby seismometer FacCiencias (East in Figure 5b and North in Figure 5c). The distance between the DAS channel and the seismometer is 300 m. We apply an automatic gain control with a 0.5-s window for display purposes. Stack 2 was generated by normalizing the rms amplitude of each stack and combining the results linked to central frequencies spanning from 4 to 16 Hz.

As mentioned in the previous paragraph, the use of separated stacks by central frequency helps to distinguish frequency bands with recurrent noise observed in stack 1. Stack 2, as shown in Figure 5-right panels, allows the filtering of noisy frequency bands (frequency higher than 22.63 Hz) or bands that do not present alignment of the seismic phases (low frequency: 2–2.83 Hz), which makes this method data adaptive. The results show different maxima corresponding to the phase alignment of the stack functions that could be interpreted as subsurface reflections. In this example, a phase arrival at 2.9 s is observed in both (DAS channel and seismometer) results (Figures 5a–5c-right panel).

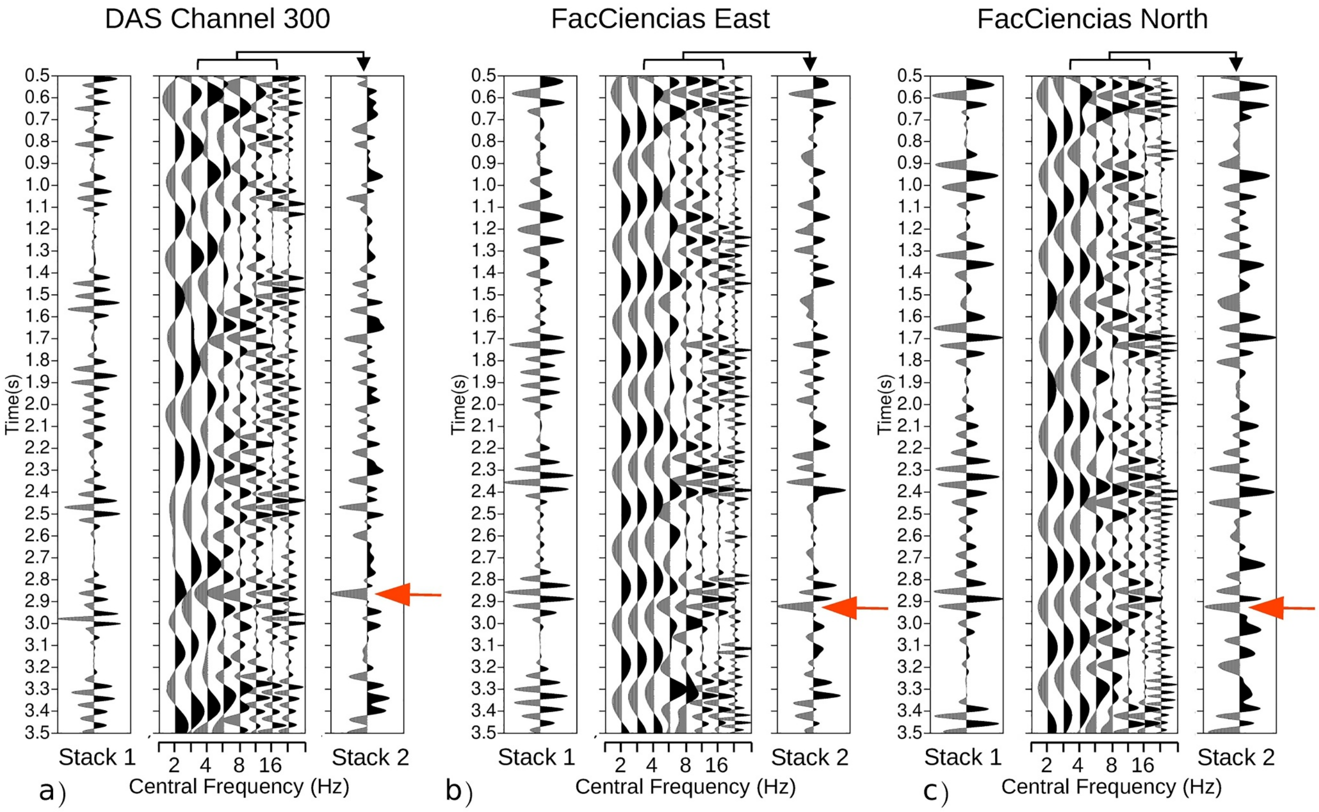

**Figure 5.** (a) Autocorrelations for DAS Channel 300: Stack of the autocorrelation functions obtained after band-pass filtering-stack 1 (left panel), stack of autocorrelations functions sorted by central frequencies used for the band-width filtering (center panel), stack 2 corresponding to central frequencies 4–16 Hz. (b, c) same as (a) but for East and North components of a conventional seismometer (FacCiencias). Red arrows mark a phase arrival observed at the three stacks 2.

21699356, 2024, 11, Downloaded from https://agupubs.onlinelibrary.wiley.com/doi/10.1029/2024JB029820 by California Institute Of Techno, Wiley Online Library on [12/11/2025]. See the Terms and Conditions (https://onlinelibrary.wiley.com/terms-and-conditions) on Wiley Online Library for rules of use; OA articles are governed by the applicable Creative Commons License

21699356, 2024, 11, Downloaded from https://agupubs.onlinelibrary.wiley.com/doi/10.1029/2024JB029820 by California Institute Of Techno, Wiley Online Library on [12/11/2025]. See the Terms and Conditions (https://onlinelibrary.wiley.com/terms-and-conditions) on Wiley Online Library for rules of use; OA articles are governed by the applicable Creative Commons License

### 4.2. Microtremor Horizontal-To-Vertical Spectral Ratio Method (MHVSR)

This method is based on the recording of ambient noise using a 3-component sensor and then calculating the ratio between the Fourier amplitude spectra of the horizontal and vertical component (MHVSR). The amplitude peaks of the MHVSR curve can be associated with the presence of seismic impedance contrasts (Molnar et al., 2022; Nakamura, 2000).

The conventional procedure for obtaining MHVSR curves involves selecting stationary windows from an extended raw recording of ambient noise using a 3C sensor. Subsequently, the Fourier amplitude spectra of all three components are computed and smoothed. The average of the horizontal components is then determined, followed by the calculation of the horizontal-to-vertical spectral ratio for each window. Finally, the average MHVSR curve, along with its standard deviation, is derived from the MHVSR curves calculated for all the selected windows.

In this study, we used 24 hr of recording time for all stations, except for the Granada D1 and Bellicena stations, where we utilized the maximum available record length of approximately 2 hr. The recordings were segmented into 250-s time windows. Since the 1990s, several researchers have introduced the MHVSR method as a valuable tool for exploration studies (e.g., Benjumea et al., 2011; Ibs-von Seht & Wohlenberg, 1999). These studies leverage the connection between the frequency corresponding to the amplitude peaks of the MHVSR curve ($f_{\mathrm{H/V}}$) and the depth ($z$) of a substantial impedance contrast (Gabàs et al., 2016). This relationship between these two parameters ($f_{\mathrm{H/V}}$ and z) incorporates the average $V_s$ of the sediment layers:

$$f_{H/V} = \frac{\overline{V_s}}{4z} \tag{1}$$

As access to $Vs$ data may not always be readily available, an alternative approach to determining $z$ involves obtaining an empirical relationship between $z$ and $f_{\mathrm{H/V}}$, as proposed by Ibs-von Seht & Wohlenberg, 1999:

$$z = af_{H/V}^{b} \tag{2}$$

where $a$ and $b$ are empirical parameters. This relationship finds support in the common observation that the shear-wave velocity of unconsolidated overburden often exhibits a velocity gradient with depth. Usually, researchers determine these empirical parameters through a process of fitting values for bedrock depth, which can be obtained from other geophysical methods or borehole logs alongside measured $f_{\mathrm{H/V}}$ values collected at the same location, to this specific relationship (Delgado et al., 2000; Gabàs et al., 2016). In this work, we follow the approach introduced in Ayala et al. (2023) that employs the velocity gradient obtained from sonic logging, in this case the one obtained Granada-D1 borehole (Figure 2). The procedure includes obtaining interval velocity of P-waves at 5-m intervals and transform the $V_p$ into $V_s$ using the relationship $V_p$–$V_s$ of Brocher (2005):

$$V_s = 0.7858 - 1.2344\ V_p + 0.7949V_p^2 - 0.1238\ V_p^3 + 0.0064\ V_p^4 \tag{3}$$

where $V_p$ and $V_s$ are in km/s.

The $V_p$ to $V_s$ transformation is one source of uncertainty that should be considered. We tested two relationships: Brocher (2005) and Greenberg and Castagna (1992). Brocher (2005) relationship was retrieved from $V_p$ and $V_s$ measurements compiled from boreholes logs, VSP, laboratory measurements and seismic refraction tomography studies from California, while Greenberg and Castagna (1992) comes from a more theoretical scenario with the use of Gassmann's equations. Since differences between estimated interval shear-wave velocities fell within a range of 78–265 m/s, we decided to use Brocher (2005) as this is the most recent reference and is based on a compilation of experimental data. Additionally, this relationship is more consistent with the one obtained in northeastern Spain for Neogene basins, which are of the same age as the Granada basin, using an independent method different from the one employed in this study (Figure 6).

We computed the average $Vs$ depth profile using the $Vs$ interval velocity, enabling us to derive a relationship between $f_{\mathrm{H/V}}$ and $z$ using Equation 1. By fitting the resultant values to Equation 2, we determined empirical coefficients a and $b$ as to be 161.82 and −1.22, respectively, with a regression sum of squares of 4.25. The difference between depth and estimated depth from the empirical relationship is less than 10 m for the Miocene

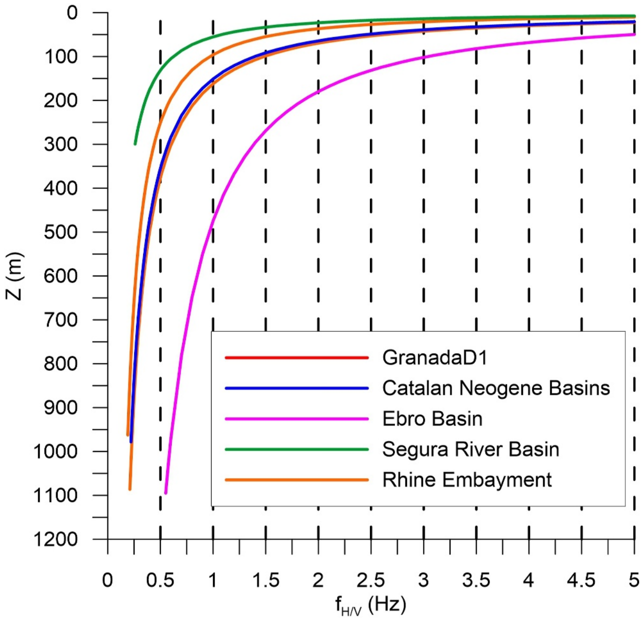

**Figure 6.** $f_{H/V}$-z relationship obtained in this study for the Granada-D1 borehole using the sonic log. For comparison, we include the relationship for the Catalan Neogene Basins (Gabàs et al., 2016) using array measurements and boreholes, the one for the Ebro Basin using a sonic log (Ayala et al., 2023), Segura River Basin using lithological logs as constraint (Delgado et al., 2000) and the Rhine Embayment relationship obtained from borehole database (Ibs-von Seth & Wohlenberg, 1999).

sediments at borehole (first 600 m). The plot of the $f_{H/V}$ -$z$ relationship is presented in Figure 6, which also displays four additional $f_{H/V}$ $z$–$h$ relationships. One was calculated for the Neogene basins situated in the Northeast of the Iberian Peninsula (Gabàs et al., 2016) referred to as Catalan Neogene Basins in Figure 6. This relationship was derived using MHVSR measurements and bedrock depth from borehole information and array measurements. The Ebro Basin relationship was obtained in the study area of Ayala et al. (2023), located in the Ebro Basin, using the same methodology we use in this study while Delgado et al. (2000) calculated a relationship for the Segura River Basin using MHVSR measurements and a borehole database. Finally, Ibs-von Seth and Wohlenberg (1999) derived an empirical relationship $f_{H/V}$ and $z$ for the Rhine Embayment in Germany.

The relationship obtained in the Granada-D1 borehole using the sonic log is very close to that obtained in the Catalan Neogene basins with the same sedimentation age. It is slightly different from the Rhine Embayment relationship, which contains a thick Quaternary soft-sediment deposit. Quaternary sediments with low shear-wave velocity characterize the Segura River Basin as denoted in the plot: for the same frequency, the Granada-D1 relationship corresponds to a deeper basement than the Segura River Basin. On the other hand, the site of the Ebro Basin relationship includes a sedimentation series from Paleogene to Triassic with older materials with higher shear-wave velocity than the Neogene Granada Basin. This is associated with deeper impedance contrasts for the same $f_{H/V}$ than those estimated using the Granada-D1 relationship. Figure 6 highlights the importance of obtaining a local $f_{H/V}$-z relationship to calculate reliable depths for the impedance contrasts. In addition, the results for different Neogene basins, Granada and Catalan basins, are very similar despite the different methodologies used to derive the relationships.

## 5. Results

### 5.1. DAS Autocorrelation

Due to the large volume of DAS data, we selected several sections along the fiber-optic cable in the city of Granada (Figure 1-yellow sections) and calculated autocorrelations with the workflow introduced in the previous section. Figures 7a–7d show the amplitude spectra for two different cable sections (channels 200 to 300 and channels 924 to 1,120, see Figure 1) for an hour, commencing at distinct times—6:00 a.m. and 3:00 p.m.—to check variations in frequency content within the DAS signal. The irregularities (random amplitude peaks) are consistent at the two different hours. A high amplitude at 80 Hz is also present for all the channels and at both in the morning and the afternoon. The origin of this dominant frequency is unknown. Other authors related the existence of discrete frequencies to electromagnetic noise coupled into mechanical sources (Cheng et al., 2023).

Figures 7e and 7f display the bandpass filter autocorrelation stacks (stack 1) for both channel sectors. Each sector has a zone that displays seismic amplitudes with spatial coherence, indicated by a red rectangle in Figure 7. The amplitude spectrum in these zones is smooth, without isolated peaks, unlike the rest of the section where the autocorrelation does not show any spatial consistency. The absence of consistent seismic amplitudes in certain zones can be attributed to the local properties of the cable (e.g., uneven coupling, cable lying loose within a pipe). This is supported by the similarity in spectra at two different times and the lack of spatial coherence in these zones. The use of amplitude spectra can also help in selecting channels with appropriate ambient noise energy for the autocorrelation procedure.

Figure 8 displays the autocorrelation results for three sectors of the fiber-optic cable (sector 1: Channels 280 to 300, sector 2: Channels 962 to 968 and sector 3: Channels 1,545 to 1,565). These sections are characterized by smooth amplitude spectra (as shown in Figure 7 for sectors 1 and 2), indicating high-quality data sets. For each sector, we show four panels. The first and second panels show the stack 1 for one channel used as reference, and for all the channels included in the sector, respectively. The stacked traces show multiple features that are

21699356, 2024, 11, Downloaded from https://agupubs.onlinelibrary.wiley.com/doi/10.1029/2024JB029820 by California Institute Of Techno, Wiley Online Library on [12/11/2025]. See the Terms and Conditions (https://onlinelibrary.wiley.com/terms-and-conditions) on Wiley Online Library for rules of use; OA articles are governed by the applicable Creative Commons License

21699356, 2024, 11, Downloaded from https://agupubs.onlinelibrary.wiley.com/doi/10.1029/2024JB029820 by California Institute Of Techno, Wiley Online Library on [12/11/2025]. See the Terms and Conditions (https://onlinelibrary.wiley.com/terms-and-conditions) on Wiley Online Library for rules of use; OA articles are governed by the applicable Creative Commons License

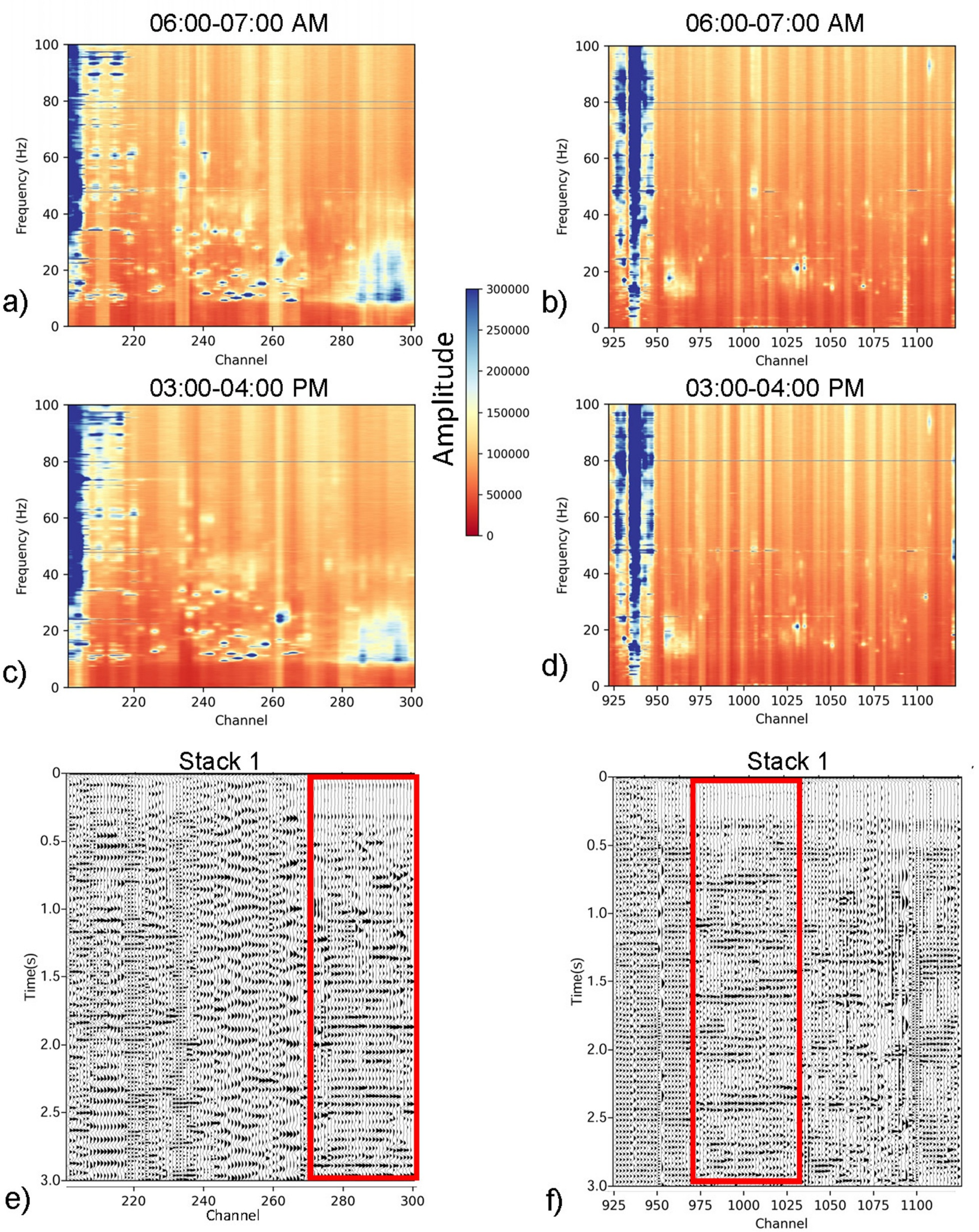

**Figure 7.** Amplitude spectra of one hour unfiltered recording for DAS channels 200 to 300 starting at 6:00 a.m. (a) and 3:00 p.m. (c) and for channels 924 to 1,120 starting at 6:00 a.m. (b) and 3:00 p.m. (d). (e, f) show the stack of the autocorrelations obtained for channels 200 to 300 and channels 924 to 1,120, respectively. Location of both sectors is shown in Figure 1. Red rectangle indicates sectors with good data quality.

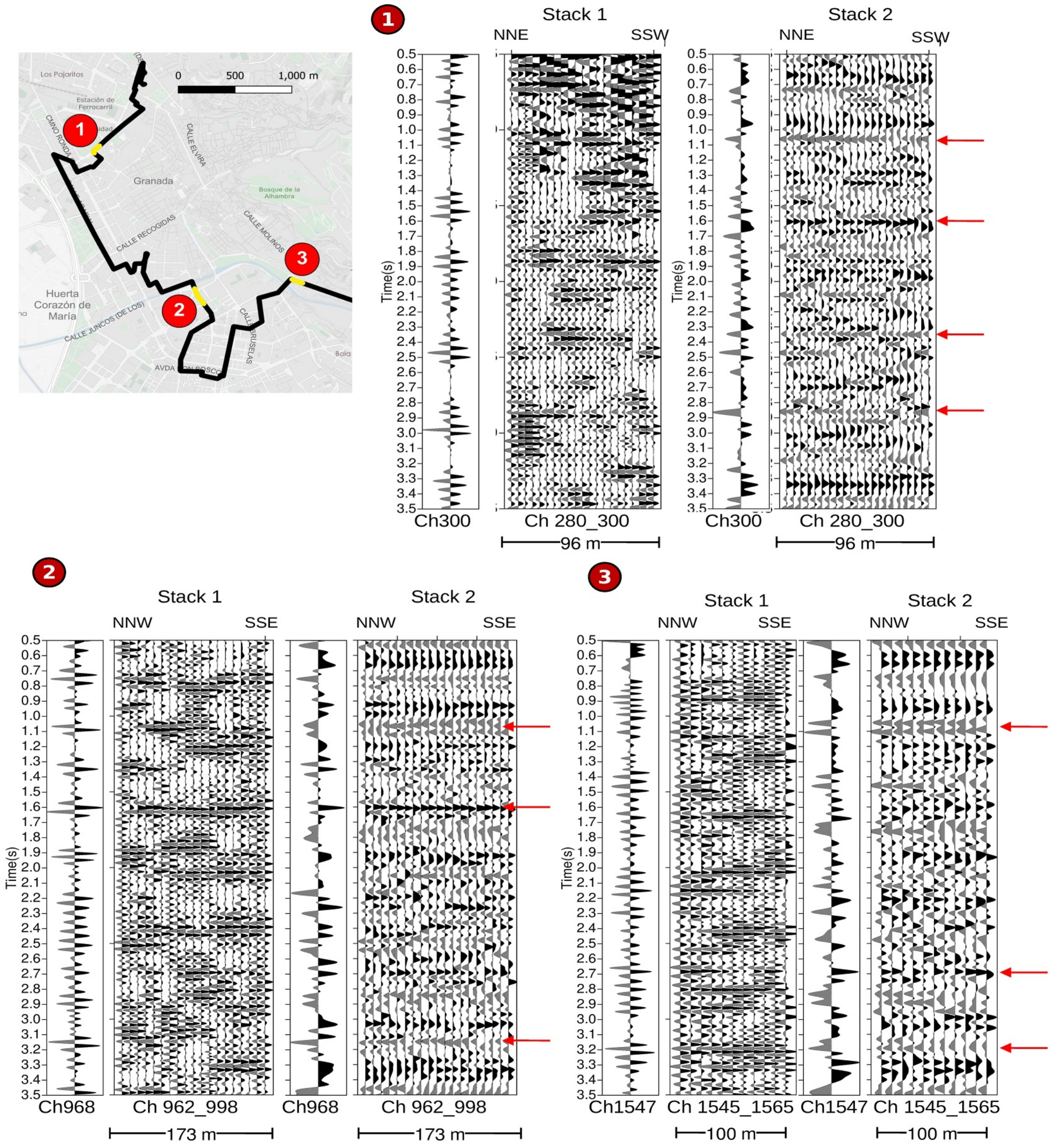

**Figure 8.** For each sector: left, autocorrelation stack calculated from data after band-pass filtering for one reference channel and for the whole sector (stack 1); right, stacks calculated for central frequencies from 4 to 16 Hz for one reference channel and for the whole sector (stack 2). The map in the upper left shows the locations of these sectors.

consistent throughout the sector. Besides the urban noise that can generate spatially consistent signals, we must keep in mind other noise sources intrinsic to the optical equipment such as: optical and electronic noise, reflectivity, and quality of the optical fiber (Li et al., 2023). To identify subsurface reflectors, we include the right two panels with the stack 2 for the reference channel and for the whole sector corresponding to central frequencies from 4 to 16 Hz (Table 1). The single channel stack helps to identify amplitude maxima that correlates with a good phase alignment through frequencies between 4 and 16 Hz. We leverage the multichannel character of DAS data set to check if these maxima are observed in the whole sector seeking for lateral consistency.

With these two constraints, we identify possible subsurface reflections at 1.1, 1.6, 2.3 and 2.9 s for Channels 280–300 and at 1.1, 1.6 and 3.1 s for Channels 962 to 998. Sector 3 presents low quality signals with a ringing aspect for the stacked traces, although potential reflections can be identified at 1.1, 2.7 and 3.2 s. This sector is located close to a very busy highway that connects the city of Granada with Sierra Nevada.

21699356, 2024, 11, Downloaded from https://agupubs.onlinelibrary.wiley.com/doi/10.1029/2024JB029820 by California Institute Of Techno, Wiley Online Library on [12/11/2025]. See the Terms and Conditions (https://onlinelibrary.wiley.com/terms-and-conditions) on Wiley Online Library for rules of use; OA articles are governed by the applicable Creative Commons License

### 5.2. Seismometers Autocorrelation

Figure 9 shows the results of applying tf-PWS method to the autocorrelograms for seven conventional seismometers of the nine locations of this study: FacCiencias, GarcLorca, ParqueCiencias, PalCong, Escolapios, EstExpZaidin and IAA (map zoom view in Figure 9 upper right panel).

Right panels show eight stack autocorrelation functions obtained after filtering around each central frequency (Table 1) while the left panels are the stacks 2. We stacked the autocorrelation stacks for central frequencies from 4 to 16 Hz in all the stations except for Escolapios, EstExpZaidin and IAA where we restricted the stack for central frequencies from 4 to 11.31 Hz due to of ringing noise at higher frequencies. We have used one horizontal component to look at S-wave reflections. The North or East component from seismometer was selected as shown in Figure 9 considering which one provides the best result.

We marked manually with red rectangles possible S-wave reflectivity changes based on consistency of a phase across at least three autocorrelation stacks corresponding to different central frequencies. For the identification of the reflections, we use that the signals should be stable over a broad frequency band and that the reflection amplitude stands out from other surrounding signals. This may happen for negative or positive amplitudes. The negative amplitudes correspond to an impedance increase at the corresponding reflector (Tibuleac & Von Seggern, 2012). The rectangles width marks which autocorrelation stacks were selected for the stack 2 shown in the right panels. Focusing on arrivals later than 2 s, FacCiencias and GarcLorca stations show a high frequency consistency in signals arriving at 2.9 s two-way travel time. These arrivals remain constant across central frequencies ranging from 2.83 to 16 Hz, thereby supporting the hypothesis that these phases correspond to subsurface reflections. ParqueCiencias and PalCongresos display some consistency around 2.8–2.85 s for the same range of central frequencies. Escolapios show some consistency at 2.6 and 3.2 s, while EstExpZaidín and IAA stations display arrivals with some coherency at different times. These arrivals do not extend beyond four frequencies, which adds uncertainty to their interpretation. However, the comparable time range of phase arrivals among neighboring stations suggests subsurface reflections, possibly corrupted by noise in a higher frequency range than the observations from the other stations.

### 5.3. Seismometers MHVSR

Figure 10 shows the average MHVSR curves and conventional deviation for three stations that were located outside the city (Granada-D1 Borehole, Belicena and IACT) and nine stations in Granada city (Figure 1). The MHVSR curve corresponding to the borehole location displays a single distinct peak at 0.31 Hz, as the lowest frequency peak, which can be related to the site fundamental frequency (Molnar et al., 2022). This peak has a high amplitude indicating a large impedance contrast. According to the lithological log, the base of the Cenozoic sediments is located at 600 m depth (Figure 2d). Using the empirical relationship $f_{H/V}$-z obtained in the Methods section, the estimated depth for the $f_{H/V}$ of Granada-D1 station is 650 m. This supports that the stratigraphic origin of this peak frequency is the basin base.

To the east and outside the city of Granada, the Belicena and IACT MHVSR curves show the lowest frequency peaks at 0.17 and 0.19 Hz, respectively. The shape of the curve is different from that obtained at the Granada-D1 borehole, with another peak around 1 Hz, which is broader for the IACT than for the Belicena MHVSR curve. Finally, the MHVSR curves for the nine stations located in Granada, display low frequency peaks ranging from 0.17 to 0.2 Hz. The MHVSR curve shapes for frequencies around 1 Hz are similar to those obtained at the IACT station, except that the curve for the Hotel station shows more irregularities. Based on the MHVSR curve obtained at the Granada D1 borehole, we interpret the lowest frequency peak obtained at the rest of the stations as the Cenozoic sediments base. The depth of this impedance contrast ranges from 1,220 to 1,400 m using the empirical relationship $f_{H/V}$-z. The stratigraphic origin of the peak around 1 Hz may be related to a significant impedance contrast within the Cenozoic sequence.

## 6. Discussion

This is the second study utilizing the DAS data set acquired with the Granada array. The first study, conducted by Li et al., in 2023, primarily focused on obtaining dispersion curves. These curves were derived using the cross-correlation of ambient noise, with the goal of constructing shear-wave velocity models for the top 100 m of the subsurface. The present work, however, extends its scope beyond the shallow subsurface. It seeks to extract

21699356, 2024, 11, Downloaded from https://agupubs.onlinelibrary.wiley.com/doi/10.1029/2024JB029820 by California Institute Of Techno, Wiley Online Library on [12/11/2025]. See the Terms and Conditions (https://onlinelibrary.wiley.com/terms-and-conditions) on Wiley Online Library for rules of use; OA articles are governed by the applicable Creative Commons License

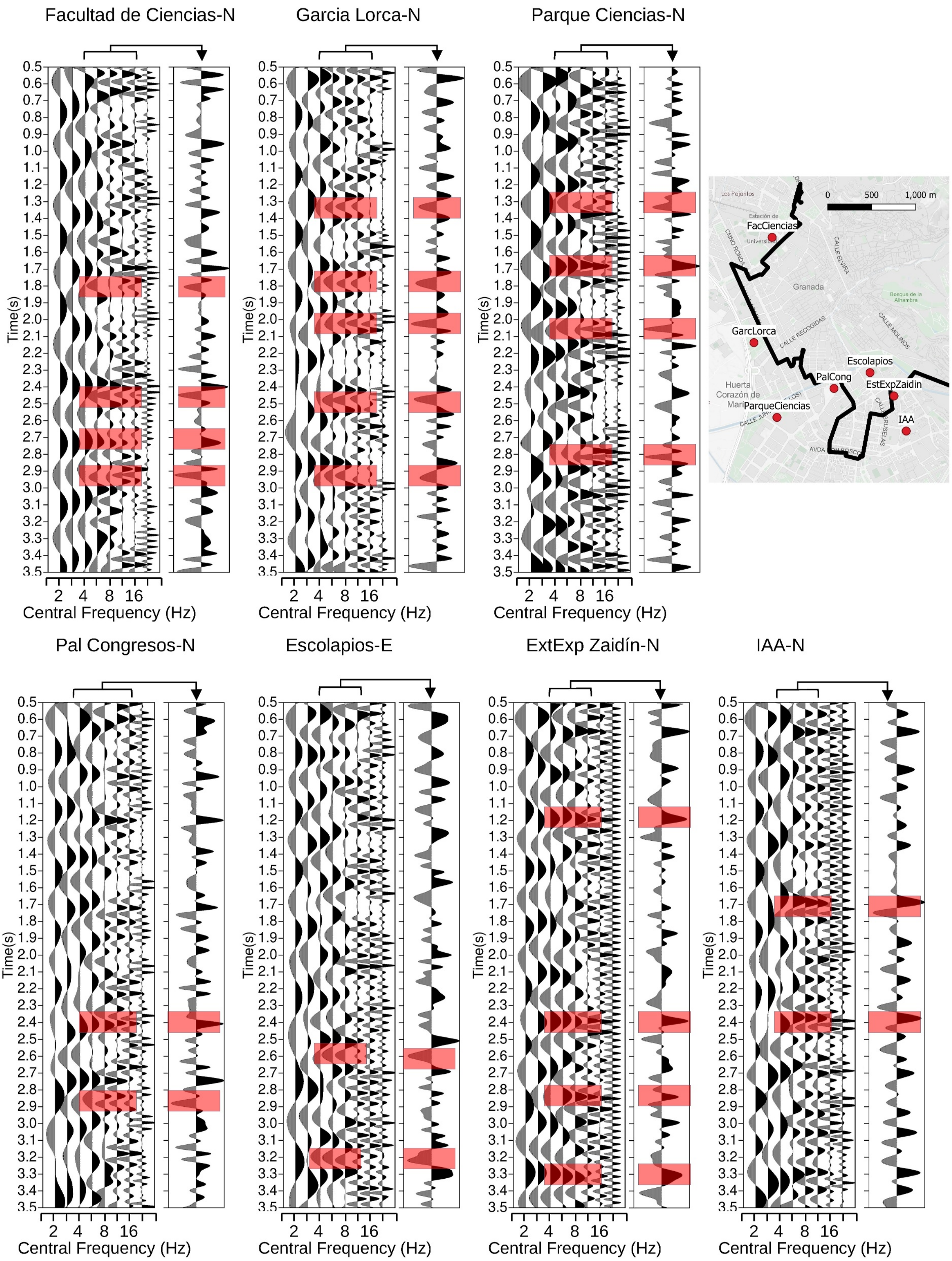

**Figure 9.** Stacked horizontal component autocorrelations for seven seismic stations in Granada. Left panels show the stacked autocorrelation functions obtained after filtering around each central frequency (Table 1) with a one-octave width filter. Right panel shows the stacks 2 for central frequencies from 4 to 16 Hz (FacCiencias, GarcLorca, ParqueCiencias and PalCongresos). For the rest of the stations, their stacks correspond to frequencies from 4 to 11.31 Hz. Red rectangles indicate arrivals with consistency across at least three central frequencies and characterize as a relative maximum at the stacks 2.

21699356, 2024, 11, Downloaded from https://agupubs.onlinelibrary.wiley.com/doi/10.1029/2024JB029820 by California Institute Of Techno, Wiley Online Library on [12/11/2025]. See the Terms and Conditions (https://onlinelibrary.wiley.com/terms-and-conditions) on Wiley Online Library for rules of use; OA articles are governed by the applicable Creative Commons License

21699356, 2024, 11, Downloaded from https://agupubs.onlinelibrary.wiley.com/doi/10.1029/2024JB029820 by California Institute Of Techno, Wiley Online Library on [12/11/2025]. See the Terms and Conditions (https://onlinelibrary.wiley.com/terms-and-conditions) on Wiley Online Library for rules of use; OA articles are governed by the applicable Creative Commons License

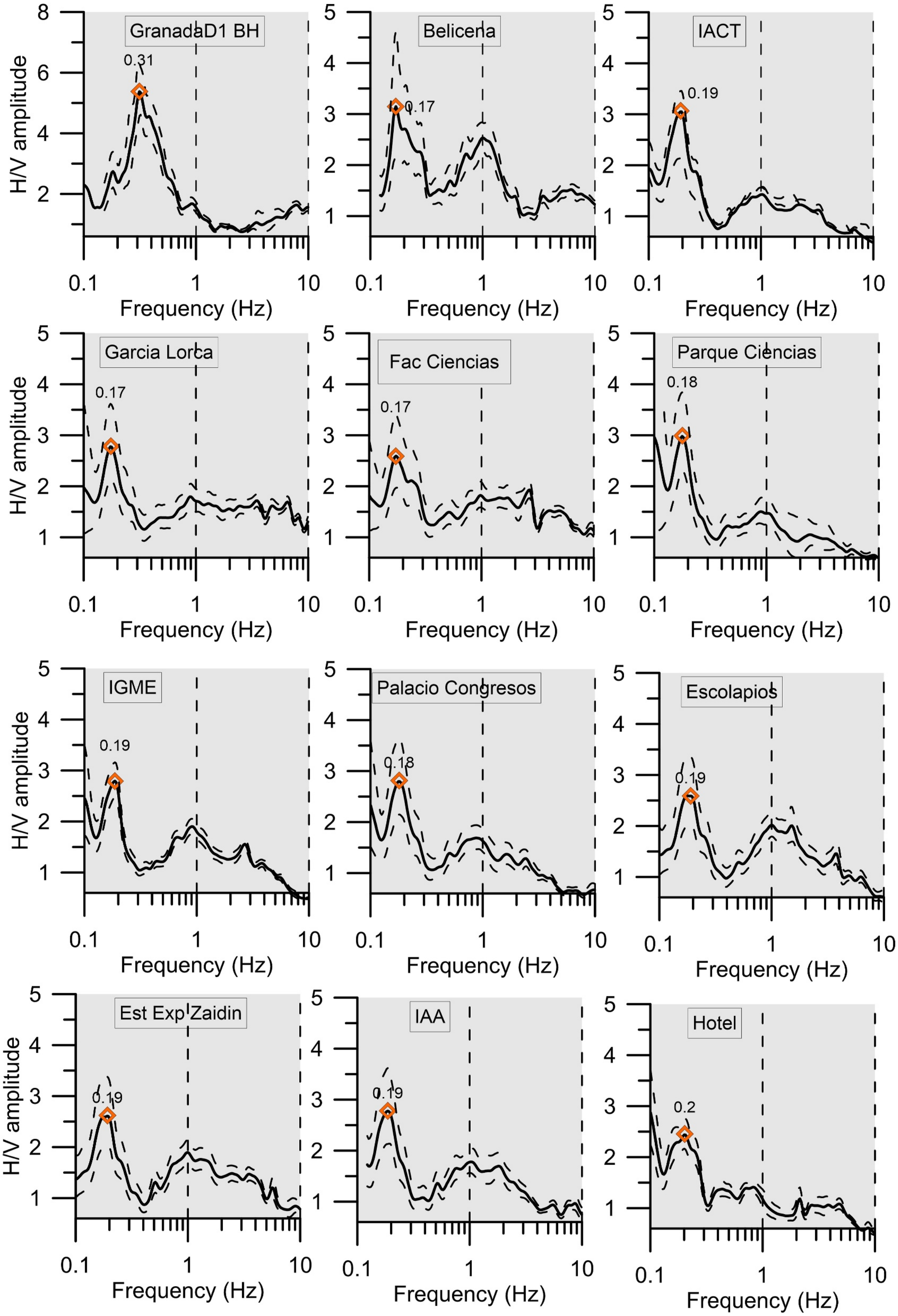

**Figure 10.** Average of MHVSR curves (continuous line) and conventional deviation (dashed lines). Maximum peak from the average MHVSR curve is denoted with an orange diamond. Amplitude scale is common for all the stations except for Granada-D1 site to optimize the peak's visibility.

21699356, 2024, 11, Downloaded from https://agupubs.onlinelibrary.wiley.com/doi/10.1029/2024JB029820 by California Institute Of Techno, Wiley Online Library on [12/11/2025]. See the Terms and Conditions (https://onlinelibrary.wiley.com/terms-and-conditions) on Wiley Online Library for rules of use; OA articles are governed by the applicable Creative Commons License

subsurface information encompassing the entire Cenozoic sequence. To achieve this, the autocorrelation method is employed. The reliability of the results obtained through autocorrelation with the DAS data set is assessed through a comparative analysis with results obtained using the autocorrelation method on conventional seismometer data sets. Additionally, the findings from the autocorrelation method are further supported by MHVSR curves.

Li et al. (2023) discuss the challenges of extracting surface wave information with the GranaDAS array. They found only nine locations to obtain high-quality dispersion images. In this study, we obtained potential good autocorrelation results in a limited number of sectors along the telecom fiber as well. One significant contributing factor to this outcome is the impact of uncertain and inconsistent cable-ground coupling on DAS data. This factor diminishes the system's ability to detect high-fidelity ground motion and renders numerous cable segments unfit for seismic measurements. Another factor already discussed in Li et al. (2023) is the geometry of the GranaDAS array. For the application of the autocorrelation technique along the fiber, differences in cable orientation relative to the predominant noise direction can produce biased results in the autocorrelation functions.

For both data sets (DAS and seismometers), the urban environment produces signals at specific frequencies created by high amplitude vibrations from engines, machinery, and public transportation—such as trams, typical in urban environments. As a result, a thorough analysis of autocorrelation results is imperative. In this study, we used the approach of comparing the stacks of autocorrelations obtained after filtering for several central frequencies based on Castro-Artola et al. (2022). In their study, the authors constrain the Moho reflection using central frequencies of approximately 0.9–2 Hz. Our target requires higher frequencies since we are studying the first 1.5–2 km of the subsurface. It is worth noting that it is more difficult to obtain subsoil information from high frequencies, especially in urban environments, inherent to the high degree of lateral heterogeneities, complicating the zero-offset reflection responses.

The autocorrelation results indicate the presence of coherent signals in both the DAS and seismometer data sets. Figure 11 focuses on the autocorrelation and MHVSR results obtained from seismometers, and Figure 12 displays the results in two DAS sectors and two seismometers located near each sector.

As the two-way travel time of an S-wave reflection is half the resonance period, the autocorrelation results can be compared to MHVSR results. For the five stations shown in Figure 11a, there is a good correlation between MHVSR and autocorrelation results. Figure 11b shows the autocorrelation stacks for the vertical components of the same five stations. There is a spatial correlation between maxima along the five stations, indicating a shallower contact toward the East in a consistent way with what is observed in the horizontal components (Figure 11a). The results provide some estimations of the $V_p/V_s$ that would be around 1.94–1.95. This would be in agreement with a study carried out during the 90s in the Granada Basin (Kagawa et al., 1996) that found average P- and S-wave velocities of 3.1 and 1.6 km/s respectively.

Regarding the MHVSR technique, Granada basin in the city shows resonance frequencies lower than 0.2 Hz that require using seismic sensors with periods higher than 5 s. In this study, the use of a suitable seismometer with sensors of 20 s is critical to obtain reliable curves. Up to date, the studies using the MHVSR technique in the urban area of Granada were restricted to frequencies higher than 0.3 Hz due to the instrumentation employed. The present study is the first one where the basement is imaged with the MHVSR method in the area.

Hence, both the autocorrelation method and the MHVSR results indicate that the identified arrivals likely represent the Cenozoic base in the city of Granada. This important subsurface feature can be estimated in terms of depth. Using the empirical relationship derived from the Granada-D1 borehole, the estimated depths of the Cenozoic base in the urban area fall within the range of 1,300–1,400 m in the stations shown in Figure 11 (from FacCiencias to PalCongresos). However, the Escolapios site displays a shallower Cenozoic base (around 1,200 m) and a wider MHVSR peak that could be related with a dipping horizon (Molnar et al., 2022). These results provide valuable insight into the subsurface structure of the region, as no previous seismic information down to the basement was previously available in the city.

Figure 12 depicts consistency between autocorrelation results in two DAS sectors and the neighboring seismometers. Specially, the negative polarity signals around 2.9 s at FacCiencias station and channels 280 to 300 and around 2.8 s at PalCongresos station and channels 962 to 998 could correspond to the Cenozoic base located at 1,300–1,400 m depth. The negative polarity would indicate velocity increase at the reflector. This negative polarity was also obtained for Moho reflections by Tibuleac and von Seggern (2012). Some of the reflections

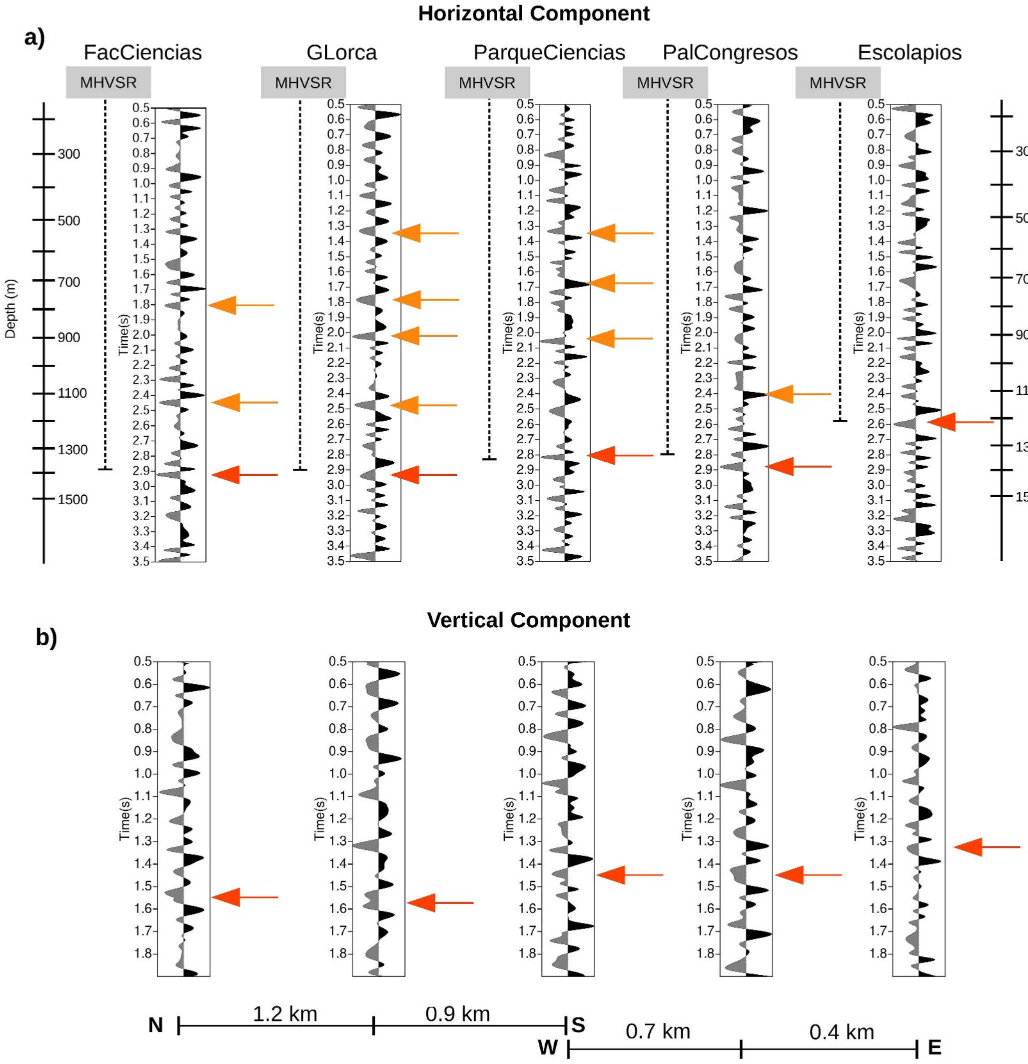

**Figure 11.** (a) Stacks two obtained for the horizontal components of five stations marking with red arrows signals probably related to Cenozoic base. Orange arrows display maxima at the stacks that could correspond to different reflections in the Cenozoic sedimentary sequence. The depth scale is calculated from the $f_{H/V}$-z relationship obtained in this work. The bottom of the vertical dashed line marks the two-way traveltime obtained from the frequency of the maxima observed at MHVSR curves (b) same as (a) for the vertical components of the same stations.

shown in Figure 12 would correspond to contacts within the Cenozoic fill, such as the calcarenite top about 200 m above the basement and, in the shallower part, seismic contrasts associated with local units (e.g., the base of the Alhambra Formation around 500 m depth).

To the authors' knowledge, this is the first study to use autocorrelation to image subsurface structures with fiber-optic data in urban areas. The support of the data set acquired with conventional seismometers has been critical. In fact, the use of some seismometers along the DAS line may help to identify the reflections in the DAS data, as the seismometer records the polarized wave field in contrast to the DAS, which records strain rate along the cable. The autocorrelation analysis approach has been successful to discern subsurface reflections for different types of artifacts in both DAS and seismometer data sets.

The use of optic fiber in urban areas provides information in zones with difficult access with seismometer data sets and generates information in a dense array of sensors. The addition of conventional 3C seismometers provides additional information about significant seismic impedance contrasts through the MHVSR technique. This information was spatially extended using the results from autocorrelation along the telecom fiber. Having a high

21699356, 2024, 11, Downloaded from https://agupubs.onlinelibrary.wiley.com/doi/10.1029/2024JB029820 by California Institute Of Techno, Wiley Online Library on [12/11/2025]. See the Terms and Conditions (https://onlinelibrary.wiley.com/terms-and-conditions) on Wiley Online Library for rules of use; OA articles are governed by the applicable Creative Commons License

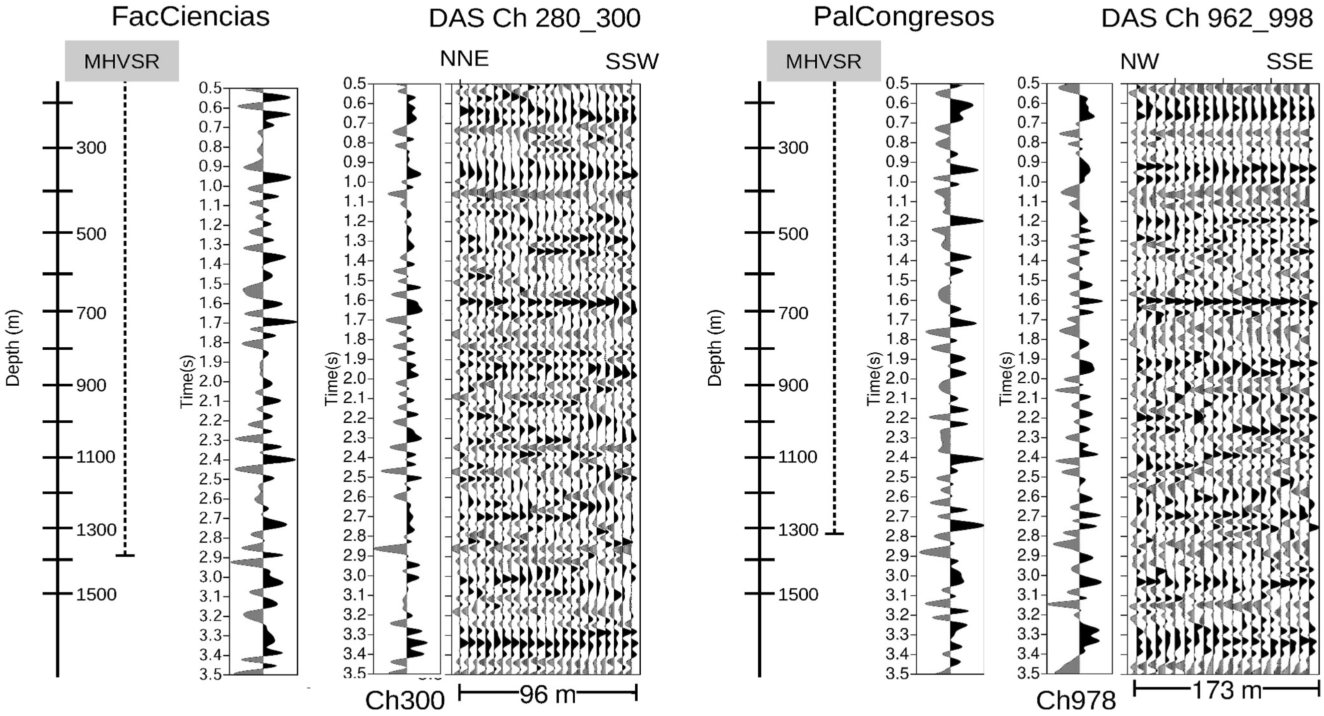

**Figure 12.** Seismometers and DAS results using autocorrelation method. MHVSR two way travel time is marked at the bottom of a vertical dashed line. Depth scale corresponds to the $f_{H/V}$-z relationship obtained at this work.

number of DAS channels facilitates the assessment of the spatial continuity of observed reflections, thereby enhancing their interpretability. The delineation of these seismic contrasts in sedimentary basins is of critical importance for groundwater studies or for seismic hazard assessment in urban areas.

## 7. Conclusions

Urban subsurface characterization by geophysical methods presents several challenges related to environmental noise or logistical constraints. The use of fiber optic cables as dense sensor arrays (DAS) has the potential to overcome the problems associated with deploying seismometers to areas where seismic information would otherwise be impossible to obtain.

In this study, we apply the autocorrelation method to a DAS data set acquired in one of the highest seismic hazardous areas in the Iberian Peninsula, Granada (Spain), for the extraction of subsurface reflections in the basin scale (1.5–2 km depth). Since this is the first instance of using this ambient noise method to image subsurface structures with fiber-optic data in urban areas, we assess the results through a comparative analysis with conventional seismometer data sets, ensuring the reliability of the autocorrelation results.

Given the significant impact of urban noise on autocorrelation results, we use a novel approach by comparing stacks of autocorrelations filtered for specific central frequencies to reveal subsurface reflections from their coherence along frequencies. We apply this analysis to DAS and seismometer data sets, the results of which confirm it as a robust method in an urban environment.

The autocorrelation results are consistent for both types of measurements. Overall, coherent S-wave reflections with two-way travel time from 2.9 to 2.6 s are identified at DAS sections and neighboring seismometers. We interpret these reflections as originated at the sediments-bedrock contact. This interpretation is confirmed by the results of MHVSR. The frequencies corresponding to MHVSR maxima obtained at the city correlates with the autocorrelation results. We calculate bedrock depth using a frequency-depth relationship calibrated at a deep borehole drilled in the basin, estimating a range from 1,200 to 1,400 m in Granada. These results are a significant outcome of this study since no previous seismic information was available down to bedrock in the urban area.

21699356, 2024, 11, Downloaded from https://agupubs.onlinelibrary.wiley.com/doi/10.1029/2024JB029820 by California Institute Of Techno, Wiley Online Library on [12/11/2025]. See the Terms and Conditions (https://onlinelibrary.wiley.com/terms-and-conditions) on Wiley Online Library for rules of use; OA articles are governed by the applicable Creative Commons License

Fiber optic cables are a common infrastructure in modern cities, making it convenient to utilize existing DAS (Distributed Acoustic Sensing) cables for urban geophysical studies. Adding a few additional seismic stations can serve as control points to reduce ambiguities and enhance the reliability of the data. Despite the uncertainties associated to DAS measurements, the findings underscore the potential of fiber-optic technology for advancing our understanding of subsurface structures in challenging urban environments, since they provide a dense subsurface coverage essential for spatial coherency assessment.

## Data Availability Statement

DAS data from the GranaDAS array are available at PubDAS (Spica et al., 2023). Three component seismic datatasets can be downloaded at Mendeley Data (Benjumea et al., 2024). Software used for autocorrelation method is available at M. Schimmel's Software Packages repository (https://diapiro.geo3bcn.csic.es/gt/mschi/SCIENCE/tseries.html; Schimmel, 1999; Schimmel & Gallart, 2007). Workflow codes were written with Python3 and Linux shell scripts. To compute the MHVSR curves, we utilized Geopsy software (http://www.geopsy.org; Wathelet et al., 2020). All the autocorrelation results have been plotted with Seismic Unix software (https://wiki.seismic-unix.org/doku.php, Stockwell, 1999). Other figures were made with Matplotlib (Caswell et al., 2020; Hunter, 2007), available under the Matplotlib licenseat https://matplotlib.org/. For the maps, we used QGIS 3.14.1-Pi (QGis Development Team, 2020). QGIS Geographic Information System. Open Source Geospatial Foundation Project. http://qgis.org.

**Acknowledgments**

This research has been funded by the ALGEMAR project (PID2021-123825OB-I00) funded by MCIN/AEI/10.13039/501100011033, with additional support from the SEASTORAGE project (TED2021-129816B-I00), funded by MCIN/AEI and the European Union NextGenerationEU/PRTR. It has also received funding from the ‘Severo Ochoa' extraordinary grants for excellence, IGME-CSIC (AECEX2021). The seismometers used in this work have been funded by EU Next Generation-within the framework of the Recovery, Transformation and Resilience Plan. We acknowledge support of the publication fee by the CSIC Open Access Publication Support Initiative through its Unit of Information Resources for Research (URICI). We are grateful to IRAM Institut de radioastronomie millimétrique in Granada for letting us to use their installations and optic fiber to acquire the data. We thank the following institutions for allowing us to install the 3C seismometer in their dependencies: Facultad de Ciencias (UGR), Parque y Fundación Federico García Lorca, Parque de las Ciencias, Instituto Andaluz de Ciencias de la Tierra (CSIC-UGR), Instituto Geológico y Minero de España—Oficina de Granada, Palacio de Congresos de Granada, Estación Experimental del Zaidin (CSIC), Instituto Astrofísica de Andalucía (CSIC), Colegio Escolapios Genil, Hotel Macía Real de la Alhambra, Centro Administrativo Parque Nacional Sierra Nevada. Thanks are given to the following people for their support in the seismometers setup: Enrique Carmona, Cecilia Morales, Teodoro Benjumea, Carlota Escutia, Blanca Bohoyo, Carlos Marin, Ana Ruiz Constan and Carlos Barceló. We are grateful to Fabian Bonilla and an anonymous reviewer for their thorough revision that helped to improve the manuscript. The manuscript also benefited from constructive comments of Associate Editor Nori Nakata and Editor Rachel Abercrombie.

## References

Ajo-Franklin, J. B., Dou, S., Lindsey, N. J., Monga, I., Tracy, C., Robertson, M., et al. (2019). Distributed acoustic sensing using dark Fiber for near-surface characterization and broadband seismic event detection. *Scientific Reports*, *9*(1), 1328. https://doi.org/10.1038/s41598-018-36675-8

Alguacil, G., Vidal, F., & Feriche, M. (2012). Site response estimation at Granada city (Southern Spain) based on deep earthquake records. In *Paper presented at the 15th world conference on earthquake engineering*.

Ayala, C., Benjumea, B., Mediato, J. F., García-Crespo, J., Clariana, P., Soto, R., et al. (2023). Developing a new innovative methodology to integrate geophysical techniques into characterization of potential $CO_2$ storage sites: Lopín structure (Southern Ebro Basin, Spain). *Geological Society, London, Special Publications*, *528*(1), 227–243. https://doi.org/10.1144/SP528-2022-70

Benjumea, B., Bohoyo, F., Mancilla, F. D. L., Almendros, J., & Carmona, E. (2024). Miniseed files from the ambient noise Granada survey acquired with 20s 3C seismometers [Dataset]. *Mendeley Data, V1*. https://doi.org/10.17632/9zcx745h4j.1

Benjumea, B., Macau, A., Gabàs, A., Bellmunt, F., Figueras, S., & Cirés, J. (2011). Integrated geophysical profiles and H/V microtremor measurements for subsoil characterization. *Near Surface Geophysics*, *9*(5), 413–425. https://doi.org/10.3997/1873-0604.2011021

Bensen, G. D., Ritzwoller, M. H., & Shapiro, N. M. (2008). Broadband ambient noise surface wave tomography across the United States. *Journal of Geophysical Research*, *113*(B5), B05306. https://doi.org/10.1029/2007JB005248

Biagioli, F., Métaxian, J. P., Stutzmann, E., Ripepe, M., Bernard, P., Trabattoni, A., et al. (2024). Array analysis of Seismo-volcanic activity with distributed acoustic sensing. *Geophysical Journal International*, *236*(1), 607–620. https://doi.org/10.1093/gji/ggad427

Bonilla, L. F., & Ben-Zion, Y. (2021). Detailed space–time variations of the seismic response of the shallow crust to small earthquakes from analysis of dense array data. *Geophysical Journal International*, *225*(1), 298–310. https://doi.org/10.1093/gji/ggaa544

Bonnefoy-Claudet, S., Cotton, F., & Bard, P. Y. (2006). The nature of noise wavefield and its applications for site effects studies: A literature review. *Earth-Science Reviews*, *79*(3–4), 205–227. https://doi.org/10.1016/j.earscirev.2006.07.004

Braga, J. C., & Cunha, P. P. (2019). Introduction. In C. Quesada & J. T. Oliveira (Eds.), *The geology of Iberia: A geodynamic approach. Regional geology reviews* (Vol. 5, pp. 1–5). Springer Nature. https://doi.org/10.1007/978-3-030-11190-8_1

Braga, J. C., Martin, J. M., & Alcala, B. (1990). Coral reefs in coarse-terrigenous sedimentary environments (upper Tortonian, Southern Spain). Sedimentary *Geology*. *Sedimentary Geology*, *66*(1–2), 135–150. https://doi.org/10.1016/0037-0738(90)90011-H

Braga, J. C., Martin, J. M., & Quesada, C. (2003). Patterns and average rates of late Neogene—Recent uplift of the Betic Cordillera, SE Spain. *Geomorphology*, *50*(1–2), 3–26. https://doi.org/10.1016/S0169-555X(02)00205-2

Brenguier, F., Shapiro, N. M., Campillo, M., Nercessian, A., & Ferrazzini, V. (2007). 3-D surface wave tomography of the Piton de la Fournaise volcano using seismic noise correlations. *Geophysical Research Letters*, *34*(2), L02305. https://doi.org/10.1029/2006GL028586

Brocher, T. M. (2005). Empirical relations between elastic wavespeeds and density in the Earth's crust. *Bulletin of the Seismological Society of America*, *95*(6), 2081–2092. https://doi.org/10.1785/0120050077

Calò, M., Di Luccio, F., Persaud, P., & Ventura, G. (2023). Ambient noise tomography of the Lipari volcanic Island (Southern Italy) from a dense nodal array. *Geophysical Research Letters*, *50*(4), e2022GL101022. https://doi.org/10.1029/2022GL101022

Castro-Artola, O., Iglesias, A., Schimmel, M., & Córdoba-Montiel, F. (2022). Moho reflections within seismic noise autocorrelations. *Journal of South American Earth Sciences*, *120*, 104080. https://doi.org/10.1016/j.jsames.2022.104080

Caswell, T., Droettboom, M., Lee, A., Hunter, J., Firing, E., Stansby, D., et al. (2020). Matplotlib v3.2.1 [Software]. *Zenodo*. https://doi.org/10.5281/zenodo.3714460

Chacón, J., Irigaray, C., El Hamdouni, R., Valverde-Palacios, I., Valverde-Espinosa, I., Calvo, F., et al. (2012). Engineering and environmental geology of Granada and its metropolitan area (Spain). *Environmental and Engineering Geoscience*, *18*(3), 217–260. https://doi.org/10.2113/gseegeosci.18.3.217

Cheng, F., Ajo-Franklin, J. B., Nayak, A., Tribaldos, V. R., Mellors, R., Dobson, P., et al. (2023). Using dark Fiber and distributed acoustic sensing to characterize a geothermal system in the Imperial Valley, Southern California. *Journal of Geophysical Research: Solid Earth*, *128*(3), e2022JB025240. https://doi.org/10.1029/2022JB025240

Clayton, R. W. (2020). Imaging the subsurface with ambient noise autocorrelations. *Seismological Research Letters*, *91*(2A), 930–935. https://doi.org/10.1785/0220190272

21699356, 2024, 11, Downloaded from https://agupubs.onlinelibrary.wiley.com/doi/10.1029/2024JB029820 by California Institute Of Techno, Wiley Online Library on [12/11/2025]. See the Terms and Conditions (https://onlinelibrary.wiley.com/terms-and-conditions) on Wiley Online Library for rules of use; OA articles are governed by the applicable Creative Commons License

Currenti, G., Allegra, M., Cannavò, F., Jousset, P., Prestifilippo, M., Napoli, R., et al. (2023). Distributed dynamic strain sensing of very long period and long period events on telecom Fiber-optic cables at Vulcano, Italy. *Scientific Reports*, *13*(1), 4641. https://doi.org/10.1038/s41598-023-31779-2

Delgado, J., López Casado, C., Estévez, A., Giner, J., Cuenca, A., & Molina, S. (2000). Mapping soft soils in the Segura River valley (SE Spain): A case study of microtremors as an exploration tool. *Journal of Applied Geophysics*, *45*(1), 19–32. https://doi.org/10.1016/S0926-9851(00)00016-1

Dou, S., Lindsey, N., Wagner, A. M., Daley, T. M., Freifeld, B., Robertson, M., et al. (2017). Distributed acoustic sensing for seismic monitoring of the near surface: A traffic-Noise interferometry case study. *Scientific Reports*, *7*(1), 11620. https://doi.org/10.1038/s41598-017-11986-4

Draganov, D., Campman, X., Thorbecke, J., Verdel, A., & Wapenaar, K. (2009). Reflection images from ambient seismic noise. *Geophysics*, *74*(5), A63–A67. https://doi.org/10.1190/1.3193529

Draganov, D., Wapenaar, K., Mulder, W., Singer, J., & Verdel, A. (2007). Retrieval of reflections from seismic background-noise measurements. *Geophysical Research Letters*, *34*(4), L04305. https://doi.org/10.1029/2006GL028735

Fang, G., Li, Y. E., Zhao, Y., & Martin, E. R. (2020). Urban near-surface seismic monitoring using distributed acoustic sensing. *Geophysical Research Letters*, *47*(6). https://doi.org/10.1029/2019GL086115

Farghal, N. S., Saunders, J. K., & Parker, G. A. (2022). The potential of using Fiber optic Distributed Acoustic Sensing (DAS) in earthquake early warning applications. *Bulletin of the Seismological Society of America*, *112*(3), 1416–1435. https://doi.org/10.1785/0120210214

Gabàs, A., Macau, A., Benjumea, B., Queralt, P., Ledo, J., Figueras, S., & Marcuello, A. (2016). Joint audio-magnetotelluric and passive seismic imaging of the Cerdanya Basin. *Surveys in Geophysics*, *37*(5), 897–921. https://doi.org/10.1007/s10712-016-9372-4

Gaite, B., Iglesias, A., Villaseñor, A., Herraiz, M., & Pacheco, J. F. (2012). Crustal structure of Mexico and surrounding regions from seismic ambient noise tomography. *Geophysical Journal International*, *188*(3), 1413–1424. https://doi.org/10.1111/j.1365-246X.2011.05339.x

Greenberg, M. L., & Castagna, J. P. (1992). Shear-wave velocity estimation in porous rocks: Theoretical formulation, preliminary verification and applications. *Geophysical Prospecting*, *40*(2), 195–209. https://doi.org/10.1111/j.1365-2478.1992.tb00371.x

Hartog, A. H. (2017). *An introduction to distributed optical fibre sensors*. CRC Press.

Hunter, J. D. (2007). Matplotlib: A 2D graphics environment [Software]. *Computing in Science & Engineering*, *9*(3), 90–95. https://doi.org/10.1109/MCSE.2007.55

Ibs-von Seht, M., & Wohlenberg, J. (1999). Microtremor measurements used to map thickness of soft sediments. *Bulletin of the Seismological Society of America*, *89*(1), 250–259. https://doi.org/10.1785/BSSA0890010250

Kagawa, T., & Group for Spanish-Japanese joint work on microzonation of Granada basin. (1996). Microtremor array observation in the Granada basin, southern Spain. In F. Vidal, M. Espinary, & J. A. Esquivel (Eds.), *Homenaje en Honor del Profesor Fernando de Miguel Martinez* (pp. 287–304). Universidad de Granada.

Konno, K., & Ohmachi, T. (1998). Ground-motion characteristics estimated from spectral ratio between horizontal and vertical components of microtremor. *Bulletin of the Seismological Society of America*, *88*(1), 228–241. https://doi.org/10.1785/BSSA0880010228

Kruiver, P. P., van Dedem, E., Romijn, R., de Lange, G., Korff, M., Stafleu, J., et al. (2017). An integrated shear-wave velocity model for the Groningen gas field, The Netherlands. *Bulletin of Earthquake Engineering*, *15*(9), 3555–3580. https://doi.org/10.1007/s10518-017-0105-y

Li, Y., Perton, M., Gaite, B., Ruiz-Barajas, S., & Spica, Z. J. (2023). Near-surface characterization using distributed acoustic sensing in an urban area: Granada, Spain. *Geophysical Journal International*, *235*(2), 1849–1860. https://doi.org/10.1093/gji/ggad331

Lin, F. C., Moschetti, M. P., & Ritzwoller, M. H. (2008). Surface wave tomography of the Western United States from ambient seismic noise: Rayleigh and love wave phase velocity maps. *Geophysical Journal International*, *173*(1), 281–298. https://doi.org/10.1111/j.1365-246X.2008.03720.x

Lindsey, N. J., Rademacher, H., & Ajo-Franklin, J. B. (2020). On the broad-band instrument response of Fiber-optic DAS arrays. *Journal of Geophysical Research*, *125*(2), e2019JB018145. https://doi.org/10.1029/2019JB018145

Lior, I., Mercerat, E. D., Rivet, D., Sladen, A., & Ampuero, J.-P. (2022). Imaging an underwater basin and its resonance modes using optical Fiber distributed acoustic sensing. *Seismological Research Letters*, *93*(3), 1573–1584. https://doi.org/10.1785/0220210349

Lior, I., Rivet, D., Ampuero, J. P., Sladen, A., Barrientos, S., Sánchez-Olavarría, R., et al. (2023). Magnitude estimation and ground motion prediction to harness Fiber optic distributed acoustic sensing for earthquake early warning. *Scientific Reports*, *13*(1), 424. https://doi.org/10.1038/s41598-023-27444-3

Lior, I., Sladen, A., Mercerat, D., Ampuero, J.-P., Rivet, D., & Sambolian, S. (2021). Strain to ground motion conversion of distributed acoustic sensing data for earthquake magnitude and stress drop determination. *Solid Earth*, *12*(6), 1421–1442. https://doi.org/10.5194/se-12-1421-2021

Lozano, L., Cantavella, J. V., Gaite, B., Ruiz-Barajas, S., Antón, R., & Barco, J. (2022). Seismic analysis of the 2020–2021 Santa Fe seismic sequence in the Granada Basin, Spain: Relocations and focal mechanisms. *Seismological Society of America*, *93*(6), 3246–3265. https://doi.org/10.1785/0220220097

Macau, A., Benjumea, B., Gabàs, A., Bellmunt, F., & Figueras, S. (2018). Geophysical measurements for site effects characterisation in the urban area of Girona, Spain. *Near Surface Geophysics*, *16*(3), 340–355. https://doi.org/10.3997/1873-0604.2018004

Madarieta-Txurruka, A., Galindo-Zaldívar, J., González-Castillo, L., Peláez, J. A., Ruiz-Armenteros, A. M., Henares, J., et al. (2021). High- and low-angle normal fault activity in a collisional Orogen: The Northeastern Granada Basin (Betic Cordillera). *Tectonics*, *40*(7), e2021TC006715. https://doi.org/10.1029/2021TC006715

Mancilla, F., Stich, D., Berrocoso, M., Martín, R., Morales, J., Fernandez-Ros, A., et al. (2013). Delamination in the Betic range: Deep structure, seismicity, and GPS motion. *Geology*, *41*(3), 307–310. https://doi.org/10.1130/g33733.1

Martin, E. R. (2018). *Passive imaging and characterization of the subsurface with distributed acoustic sensing*. PhD thesis. Department of Geophysics, Stanford University.

Martin, E. R., Lindsey, N., Ajo-Franklin, J., & Biondi, B. (2021). Introduction to interferometry of Fiber-optic strain Measurements. In *Distributed acoustic sensing in geophysics: Methods and applications* (pp. 111–129). American Geophysical Union.

Martín, R., Stich, D., Morales, J., & Mancilla, F. (2015). Moment tensor solutions for the Iberian-Maghreb region during the IberArray deployment (2009–2013). *Tectonophysics*, *663*, 261–274. https://doi.org/10.1016/j.tecto.2015.08.012

Molnar, S., Sirohey, A., Assaf, J., Bard, P. Y., Castellaro, S., Cornou, C., et al. (2022). A review of the Microtremor Horizontal-to-Vertical Spectral Ratio (MHVSR) method. *Journal of Seismology*, *26*(4), 653–685. https://doi.org/10.1007/s10950-021-10062-9

Morales, J., Serrano, I., Vidal, F., & Torcal, F. (1997). The depth of the earthquake activity in the Central Betics (Southern Spain). *Geophysical Research Letters*, *24*(24), 3289–3292. https://doi.org/10.1029/97GL03306

Morales, J., Vidal, F., De Miguel, F., Alguacil, G., Posadas, A. M., Ibáñez, J. M., et al. (1990). Basement structure of the Granada basin, Betic cordilleras, southern Spain. *Tectonophysics*, *177*(4), 337–348. https://doi.org/10.1016/0040-1951(90)90394-N

Muñoz, D., Cisternas, A., Udıas, A., Mezcua, J., De Galdeano, C. S., Morales, J., et al. (2002). Microseismicity and tectonics in the Granada Basin (Spain). *Tectonophysics*, *356*(4), 233–252. https://doi.org/10.1016/S0040-1951(02)00338-4

21699356, 2024, 11, Downloaded from https://agupubs.onlinelibrary.wiley.com/doi/10.1029/2024JB029820 by California Institute Of Techno, Wiley Online Library on [12/11/2025]. See the Terms and Conditions (https://onlinelibrary.wiley.com/terms-and-conditions) on Wiley Online Library for rules of use; OA articles are governed by the applicable Creative Commons License

Nakamura, Y. (2000). Clear identification of fundamental idea of Nakamura's technique and its applications. In *Paper presented at 12th world conference on earthquake Engineering*.

Nakata, N., Chang, J. P., Lawrence, J. F., & Boué, P. (2015). Body-wave extraction and tomography at Long Beach, California, with ambient-noise tomography. *Journal of Geophysical Research: Solid Earth*, *120*(2), 1159–1173. https://doi.org/10.1002/2015JB011870

Nocquet, J. M. (2012). Present-day kinematics of the Mediterranean: A comprehensive overview of GPS results. *Tectonophysics*, *579*(5), 220–242. https://doi.org/10.1016/j.tecto.2012.03.037

Palano, M., González, P. J., & Fernández, J. (2015). The Diffuse Plate boundary of Nubia and Iberia in the Western Mediterranean: Crustal deformation evidence for viscous coupling and fragmented lithosphere. *Earth and Planetary Science Letters*, *430*, 439–447. https://doi.org/10.1016/j.epsl.2015.08.040

Perton, M., Spica, Z., & Caudron, C. (2018). Inversion of the horizontal to vertical spectral ratio in presence of strong lateral heterogeneity. *Geophysical Journal International*, *212*(2), 930–941. https://doi.org/10.1093/gji/ggx458

Poli, P., Campillo, M., Pedersen, H., & Group, L. W. (2012). Body-wave imaging of Earth's mantle discontinuities from ambient seismic noise. *Science*, *338*(6110), 1063–1065. https://doi.org/10.1126/science.122819

QGIS Development Team. (2020). QGIS geographic information system [Software]. *QGIS Association*. Retrieved from https://www.qgis.org

Qin, L., Qiu, H., Nakata, N., Deng, S., Levander, A., & Ben-Zion, Y. (2023). Variable daily autocorrelation functions of high-frequency seismic data on Mars. *Seismological Research Letters*, *94*(2A), 746–758. https://doi.org/10.1785/0220220196

Rodríguez-Fernández, J., & De Galdeano, C. S. (2006). Late orogenic intramontane basin development: The Granada basin, Betics (Southern Spain). *Basin Research*, *18*(1), 85–102. https://doi.org/10.1111/j.1365-2117.2006.00284.x

Romero, P., & Schimmel, M. (2018). Mapping the basement of the Ebro Basin in Spain with seismic ambient noise autocorrelations. *Journal of Geophysical Research: Solid Earth*, *123*(6), 5052–5067. https://doi.org/10.1029/2018JB015498

Sánchez-Sesma, F. J., Rodríguez, M., Iturrarán-Viveros, U., Luzón, F., Campillo, M., Margerin, L., et al. (2011). A theory for Microtremor H/V spectral ratio: Application for a layered medium. *Geophysical Journal International*, *186*(1), 221–225. https://doi.org/10.1111/j.1365-246X.2011.05064.x

Sanz de Galdeano, C., García Tortosa, F. J., Peláez Montilla, J. A., Alfaro García, P., Azañón, J. M., Galindo Zaldívar, J., et al. (2012). Main active faults in the Granada and Guadix-Baza basins (Betic Cordillera). *Journal of Iberian Geology*, *38*(1), 209–223. https://doi.org/10.5209/rev_JIGE.2012.v38.n1.39215

Schimmel, M. (1999). Phase cross-correlations: Design, comparisons and applications [Software]. *Bulletin of the Seismological Society of America*, *89*(5), 1366–1378. https://doi.org/10.1785/BSSA0890051366

Schimmel, M., & Gallart, J. (2007). Frequency-dependent phase coherence for noise suppression in seismic array data [Software]. *Journal of Geophysical Research*, *112*(B4), B04303. https://doi.org/10.1029/2006JB004680

Schimmel, M., Stutzmann, E., Lognonné, P., Compaire, N., Davis, P., Drilleau, M., et al. (2021). Seismic noise autocorrelations on Mars. *Earth and Space Science*, *8*(6), e2021EA001755. https://doi.org/10.1029/2021EA001755

Serpelloni, E., Vannucci, G., Pondrelli, S., Argnani, A., Casula, C., Anzidei, M., et al. (2007). Kinematics of the Western Africa–Eurasia plate boundary from focal mechanisms and GPS data. *Geophysical Journal International*, *169*(3), 1180–1200. https://doi.org/10.1111/j.1365-246X.2007.03367.x

Serrano, I., Bohoyo, F., Galindo-Zaldívar, J., Morales, J., & Zhao, D. (2002). Geophysical signatures of a basic-body rock placed in the upper crust of the External Zones of the Betic Cordillera (Southern Spain). *Geophysical Research Letters*, *29*(11), 18. https://doi.org/10.1029/2001GL013487

Serrano, I., Morales, J., Zhao, D., Torcal, F., & Vidal, F. (1998). P-wave tomographic images in the Central Betics-Alborán Sea (South Spain) using local earthquakes: Contribution for a continental collision. *Geophysical Research Letters*, *25*(21), 4031–4034. https://doi.org/10.1029/1998GL900021

Shapiro, N. M., & Campillo, M. (2004). Emergence of broadband Rayleigh waves from correlations of the ambient seismic noise. *Geophysical Research Letters*, *31*(7), L07614. https://doi.org/10.1029/2004GL019491

Shragge, J., Yang, J., Issa, N., Roelens, M., Dentith, M., & Schediwy, S. (2021). Low-frequency ambient Distributed Acoustic Sensing (DAS): Case study from Perth, Australia. *Geophysical Journal International*, *226*(1), 564–581. https://doi.org/10.1093/gji/ggab111

Sladen, A., Rivet, D., Ampuero, J. P., De Barros, L., Hello, Y., Calbris, G., & Lamare, P. (2019). Distributed sensing of earthquakes and ocean-solid Earth interactions on seafloor telecom cables. *Nature Communications*, *10*(1), 5777. https://doi.org/10.1038/s41467-019-13793-z

Spica, Z. J., Ajo-Franklin, J., Beroza, G. C., Biondi, B., Cheng, F., Gaite, B., et al. (2023). PubDAS: A PUBlic distributed acoustic sensing datasets repository for geosciences [Dataset]. *Seismological Research Letters*, *94*(2 A), 983–998. https://doi.org/10.1785/0220220279

Spica, Z. J., Nishida, K., Akuhara, T., Pétrélis, F., Shinohara, M., & Yamada, T. (2020). Marine sediment characterized by ocean-bottom Fiber-optic seismology. *Geophysical Research Letters*, *47*(16), e2020GL088360. https://doi.org/10.1029/2020GL088360

Spica, Z. J., Perton, M., Martin, E. R., Beroza, G. C., & Biondi, B. (2020). Urban seismic site characterization by Fiber-optic seismology. *Journal of Geophysical Research: Solid Earth*, *125*(3), e2019JB018656. https://doi.org/10.1029/2019JB018656

Stehly, L., Fry, B., Campillo, M., Shapiro, N. M., Guilbert, J., Boschi, L., & Giardini, D. (2009). Tomography of the Alpine region from observations of seismic ambient noise. *Geophysical Journal International*, *178*(1), 338–350. https://doi.org/10.1111/j.1365-246X.2009.04132.x

Stich, D., Martínez-Solares, J. M., Custódio, S., Batlló, J., Martín, R., Teves-Costa, P., & Morales, J. (2020). Seismicity of the Iberian Peninsula. In C. Quesada & J. T. Oliveira (Eds.), *The geology of Iberia: A geodynamic approach. Regional geology reviews* (Vol. 5, pp. 11–32). Springer Nature. https://doi.org/10.1007/978-3-030-10931-8_3

Stockwell, J. W. Jr. (1999). The CWP/SU: Seismic Un∗ x package [Software]. *Computers & Geosciences*, *25*(4), 415–419. https://doi.org/10.1016/S0098-3004(98)00145-9

Tibuleac, I. M., & von Seggern, D. (2012). Crust-mantle boundary reflectors in Nevada from ambient seismic noise autocorrelations. *Geophysical Journal International*, *189*(1), 493–500. https://doi.org/10.1111/j.1365-246X.2011.05336.x

Ugalde, A., Becerril, C., Villaseñor, A., Ranero, C. R., Fernández-Ruiz, M. R., Martin-Lopez, S., et al. (2022). Noise levels and signals observed on submarine Fibers in the Canary Islands using DAS. *Seismological Research Letters*, *93*(1), 351–363. https://doi.org/10.1785/0220210049

Ugalde, A., Gaite, B., & Villaseñor, A. (2014). Temporal variations of seismic velocity at paradox valley, Colorado, using passive image interferometry. *Bulletin of the Seismological Society of America*, *104*(3), 1088–1099. https://doi.org/10.1785/0120130133

Wathelet, M., Chatelain, J.-L., Cornou, C., Di Giulio, G., Guillier, B., Ohrnberger, M., & Savvaidis, A. (2020). Geopsy: A user-friendly open-source tool set for ambient vibration processing [Software]. *Seismological Research Letters*, *91*(3), 1878–1889. https://doi.org/10.1785/0220190360

Wuestefeld, A., Spica, Z. J., Aderhold, K., Huang, H. H., Ma, K. F., Lai, V. H., et al. (2023). The global DAS month of February 2023. *Seismological Research Letters*, *95*(3), 1569–1577. https://doi.org/10.1785/0220230180

21699356, 2024, 11, Downloaded from https://agupubs.onlinelibrary.wiley.com/doi/10.1029/2024JB029820 by California Institute Of Techno, Wiley Online Library on [12/11/2025]. See the Terms and Conditions (https://onlinelibrary.wiley.com/terms-and-conditions) on Wiley Online Library for rules of use; OA articles are governed by the applicable Creative Commons License

Yang, Y., Ritzwoller, M. H., & Jones, C. H. (2011). Crustal structure determined from ambient noise tomography near the magmatic Centers of the Coso region, Southeastern California. *Geochemistry, Geophysics, Geosystems*, *12*(2), Q02009. https://doi.org/10.1029/2010GC003362

Yao, H., van der Hilst, R. D., & de Hoop, M. V. (2006). Surface-wave array tomography in SE Tibet from ambient seismic noise and two-station analysis-I, Phase velocity maps. *Geophysical Journal International*, *166*(2), 732–744. https://doi.org/10.1111/j.1365-246X.2006.03028.x

Yin, J., Zhu, W., Li, J., Biondi, E., Miao, Y., Spica, Z. J., et al. (2023). Earthquake magnitude with DAS: A transferable data-based scaling relation. *Geophysical Research Letters*, *50*(10), e2023GL103045. https://doi.org/10.1029/2023GL103045

Zeng, X., Lancelle, C., Thurber, C., Fratta, D., Wang, H., Lord, N., et al. (2017). Properties of noise cross-correlation functions obtained from a distributed acoustic sensing array at Garner Valley, California. *Bulletin of the Seismological Society of America*, *107*(2), 603–610. https://doi.org/10.1785/0120160168

Zhan, Z. (2019). Distributed acoustic sensing turns Fiber-optic cables into sensitive seismic antennas. *Seismological Research Letters*, *91*(1), 1–15. https://doi.org/10.1785/0220190112

21699356, 2024, 11, Downloaded from https://agupubs.onlinelibrary.wiley.com/doi/10.1029/2024JB029820 by California Institute Of Techno, Wiley Online Library on [12/11/2025]. See the Terms and Conditions (https://onlinelibrary.wiley.com/terms-and-conditions) on Wiley Online Library for rules of use; OA articles are governed by the applicable Creative Commons License